

# JGR Atmospheres

## RESEARCH ARTICLE

10.1029/2024JD042984

### Key Points:

- The CE318-T photometer has a unique ability to measure nocturnal aerosol optical parameters under a wide range of moon's illumination in Ayvaj
- Both AODs and the Ångström exponent exhibit a prominent diurnal variation, and nocturnal AOD values show a good continuity with daytime AODs
- Dust AODs in Ayvaj show negative percentage departures in daytime and positive departures in nighttime while AEs show an opposite pattern

### Correspondence to:

J. Bi,  
bjjr@lzu.edu.cn

### Citation:

Bi, J., Wang, X., Huang, Z., Abdullaev, S. F., Li, B., Meng, Z., et al. (2025). Diurnal and nocturnal dust aerosol characteristics at Ayvaj of southwest Tajikistan determined from sun-sky-lunar photometric measurements. *Journal of Geophysical Research: Atmospheres*, 130, e2024JD042984. <https://doi.org/10.1029/2024JD042984>

Received 20 NOV 2024

Accepted 13 FEB 2025

### Author Contributions:

**Conceptualization:** Jianrong Bi,

Jianping Huang

**Data curation:** Jianrong Bi, Xiting Wang,

Zhongwei Huang, Sabur F. Abdullaev,

Zhaozhao Meng, Dilovar Nozirov

**Formal analysis:** Jianrong Bi,

Xiting Wang

**Funding acquisition:** Jianrong Bi,

Xiting Wang, Zhongwei Huang,

Jianping Huang

**Investigation:** Jianrong Bi, Xiting Wang,

Zhongwei Huang, Sabur F. Abdullaev,

Jianping Huang

**Methodology:** Jianrong Bi, Xiting Wang,

Zhongwei Huang, Sabur F. Abdullaev,

Bowen Li

**Project administration:** Jianrong Bi

**Resources:** Jianrong Bi, Xiting Wang,

Zhongwei Huang, Sabur F. Abdullaev

**Software:** Jianrong Bi, Xiting Wang,

Bowen Li

**Supervision:** Jianrong Bi

**Validation:** Jianrong Bi, Xiting Wang,

Sabur F. Abdullaev, Jianping Huang

## Diurnal and Nocturnal Dust Aerosol Characteristics at Ayvaj of Southwest Tajikistan Determined From Sun-Sky-Lunar Photometric Measurements

Jianrong Bi<sup>1,2,3</sup> , Xiting Wang<sup>1,2,3</sup> , Zhongwei Huang<sup>1,2,3</sup> , Sabur F. Abdullaev<sup>4</sup> , Bowen Li<sup>5</sup>,  
Zhaozhao Meng<sup>1,2,3</sup> , Dilovar Nozirov<sup>4</sup> , and Jianping Huang<sup>1,2,3</sup> 

<sup>1</sup>Key Laboratory for Semi-Arid Climate Change of the Ministry of Education, College of Atmospheric Sciences, Lanzhou University, Lanzhou, China, <sup>2</sup>Collaborative Innovation Center for Western Ecological Safety, Lanzhou University, Lanzhou, China, <sup>3</sup>Gansu Provincial Field Scientific Observation and Research Station of Semi-arid Climate and Environment, Lanzhou, China, <sup>4</sup>Physical-Technical Institute, Academy of Sciences of Republic of Tajikistan, Dushanbe, Tajikistan, <sup>5</sup>Lanzhou Regional Climate Center, Lanzhou, China

**Abstract** Based on CE318-T sun-sky-lunar photometric measurements, this study examined the diurnal and nocturnal variations of dust aerosol characteristics from June to October 2023 at Ayvaj of southwest Tajikistan for the first time. The results indicated that the ROLO-RCF (RObotic Lunar Observatory model with correction factor)-modified method was capable of reliably calculating nocturnal aerosol optical depths (AODs) and the Ångström exponent ( $AE_{440-870\text{ nm}}$ ) measured from the CE318-T photometer, which was validated with synchronous observations of a lidar. The AOD day/night transition coherence test has firmly demonstrated the reliability of nighttime AODs obtained from a photometer at night-to-day and day-to-night time intervals. Both spectral AOD values and  $AE_{440-870\text{ nm}}$  exhibited prominent diurnal variations, and nocturnal AODs showed a good continuity with daytime AODs in a wide range of moon's illuminations. The maximal  $AOD_{500\text{ nm}}$ ,  $PM_{2.5}$  and  $PM_{10}$  mass concentrations under a heavy dust event on 9–10 June, 2023 were 3.07, 2,800 and 9,400  $\mu\text{g}/\text{m}^3$ , respectively, and corresponding  $AE_{440-870\text{ nm}}$ , fine-mode fraction, and ratio of  $PM_{2.5}/PM_{10}$  were 0.01, 0.17 and 0.24, respectively, implying the dominance of large desert dust particles in Ayvaj. The percentage departures of  $AOD_{500\text{ nm}}$  showed systematically negative values ( $-22\% \sim -5\%$ ) during daytime and positive values ( $+6\% \sim +25\%$ ) in nighttime and corresponding  $AE_{440-870\text{ nm}}$  ranged within  $\pm 25\%$ , attributable to the frequent intrusion of dust events. Both daytime and nighttime AODs showed a similar monthly variation characteristic, and average AOD values ( $AOD_{440\text{ nm}}$  of 0.25  $\sim$  0.51) in prevailing dust seasons were generally greater than the ones ( $AOD_{440\text{ nm}}$  of 0.16  $\sim$  0.45) in September and October. In contrast, the monthly average  $AE_{440-870\text{ nm}}$  exhibited an opposite pattern. The overall average daytime and nighttime  $AOD_{440\text{ nm}}$  values were  $0.327 \pm 0.187$  and  $0.381 \pm 0.135$ , respectively, and corresponding  $AE_{440-870\text{ nm}}$  were  $0.472 \pm 0.192$  and  $0.467 \pm 0.200$ , respectively, suggesting that coarse-mode dust particles were the main contributors to total aerosol loading in Ayvaj. In summary, this paper has verified that the CE318-T photometer had a unique capability to measure nocturnal aerosol optical parameters under a wide range of lunar phase cycles in Ayvaj. Such significant diurnal variability of dust AODs and  $AE_{440-870\text{ nm}}$  disparity should be included in regional climate models to simulate its diurnal radiative effect in the future work.

**Plain Language Summary** Diurnal variability of aerosol optical property is essential to validate satellite aerosol products, assess its public health, climate radiative forcing and eco-environmental impacts. For the first time, this study investigated the diurnal and nocturnal cycles of dust aerosol characteristics at Ayvaj of southwest Tajikistan determined from CE318-T sun-sky-lunar photometric measurements. We found that CE318-T photometer had a unique capability to measure nocturnal aerosol optical parameters under a wide range of moon's illuminations in Ayvaj. Both spectral aerosol optical depths (AODs) and the Ångström exponent ( $AE_{440-870\text{ nm}}$ ) exhibited a prominent diurnal variation, and nocturnal AOD values presented a good continuity with daytime AODs under different aerosol loading levels. The percentage departures of dust  $AOD_{500\text{ nm}}$  were negative values in daytime and positive values in nighttime, and corresponding  $AE_{440-870\text{ nm}}$  showed an opposite pattern, depending on emission sources and meteorological conditions. Such significant diurnal variability of dust AODs and  $AE_{440-870\text{ nm}}$  should be included in regional climate models to simulate its diurnal radiative effect in the future work.

**Visualization:** Jianrong Bi, Xiting Wang, Zhaozhao Meng

**Writing – original draft:** Jianrong Bi, Xiting Wang

**Writing – review & editing:** Jianrong Bi, Xiting Wang, Zhongwei Huang, Sabur F. Abdullaev, Bowen Li, Zhaozhao Meng, Dilovar Nozirov, Jianping Huang

## 1. Introduction

Aerosol particles in the troposphere exhibit great temporal variation and spatial distribution patterns, which are regulated by diverse emission sources, meteorological diffusion conditions, chemical reactions, transport, and scavenging processes (Smirnov et al., 2002; Zhang et al., 2012). Aerosol optical depth (AOD) and the Ångström exponent (AE) are two pivotal physical parameters to represent the columnar aerosol loading and size/type and directly determine the magnitude of radiative forcing, and thus have a substantial influence on air quality and climate change. The diurnal variability of aerosol optical property is crucial to validate geostationary satellite aerosol products (Chen et al., 2025; Liu et al., 2024; Zhang et al., 2012); predict surface particulate matter concentrations (Ma et al., 2024); and accurately assess its climatology, direct radiative forcing, and eco-environmental impacts (Arola et al., 2013; Wang et al., 2015; Yu et al., 2004), as well as elucidate the complex interactions between aerosols and clouds (Che et al., 2024; Kuang et al., 2015; Li et al., 2022). Smirnov et al. (2002) analyzed the diurnal cycle of daytime AOD at diverse sites around the world derived from multiyear AEROSOL ROBOTIC NETWORK (AERONET) products and showed that diurnal changes varied from 10% to 40% over various urban/industrial areas, mainly relying on aerosol types and landscapes. Wang et al. (2004) examined the diurnal variability of dust aerosol properties from 1999 to 2000 at Dunhuang in Northwest China based on sky radiometer's observations and revealed that both AOD and  $AE_{440-870\text{ nm}}$  indicated a remarkable daytime change with  $-8\% \sim 8\%$  and  $-25\% \sim 15\%$ , respectively. Zhang et al. (2012) explored the aerosol daytime variations over North and South America obtained from a multiyear AERONET AOD data sets and manifested a wide range of daytime change of AOD and  $AE_{440-870\text{ nm}}$ , depending on location and dominant aerosol species. Arola et al. (2013) have verified that the overall impacts of daytime AOD cycles averaged over all AERONET sites on 24-hr aerosol direct radiative forcing (ADRF) were smaller at the top of atmosphere (TOA,  $\pm 0.1 \sim \pm 0.2\text{ Wm}^{-2}$ ), but there were much stronger impacts in individual sites ( $-0.83 \sim +1.12\text{ Wm}^{-2}$ ). Christopher et al. (2003) also manifested that if diurnal changes in aerosol optical depth (low dust loading with AOD of  $0.26 \pm 0.13$ ) were not considered, it would result in uncertainties in shortwave ADRF of  $4\text{ Wm}^{-2}$  at the surface and  $2\text{ Wm}^{-2}$  at TOA. Song et al. (2018) have demonstrated that the daytime AOD departures at 18 stations in northern China ranged from  $-30.26\%$  to  $30.28\%$ , which led to an underestimation of annual averaged ADRF at the surface and TOA was  $-0.17$  and  $-0.03\text{ Wm}^{-2}$ , respectively, if daytime variations of AOD and  $AE_{440-870\text{ nm}}$  were replaced by the daily mean value in northern China Plain. These impressive findings are fruitful to greatly improve our understanding of climatic and environmental influences of tropospheric aerosol on both regional and global scales. However, the earlier works were primarily dedicated to surveying the daytime variability of aerosol loading due to the constraint of detection technique, and there is still an acute paucity of nocturnal AOD measurements (Berkoff et al., 2011; Bi et al., 2024). Nighttime AOD data sets are essential to fully unravel the complete diurnal variations of aerosol optical properties (Barreto et al., 2017, 2019; Román et al., 2020), nocturnal new particle formation (Kulmala et al., 2013), accumulation of air pollutants at nighttime (X. Huang et al., 2018; Li et al., 2017), and aerosol longwave radiative effect (Rosenfeld et al., 2008; Tao et al., 2012) at high latitude regions during prolonged darkness in winter (Baibakov et al., 2015; Zhang et al., 2008). Thereby, a comprehensive knowledge of daytime and nocturnal aerosol optical characteristics is pivotal to accurately evaluate their public health effect, diurnal exposure, climatic impacts, and transboundary transport.

Tajikistan is located on an important dust transport route of the global dust belt (Hofer et al., 2017; Xi & Sokolik, 2016) that frequently suffers from the intrusion of dust storms every summer and autumn seasons (Abdullaev & Sokolik, 2019; Golitsyn & Gillette, 1993). Airborne dust particles can not only severely degrade atmospheric visibility, deteriorate air quality, and lead to serious respiratory diseases and cardiopulmonary mortality (Zhang et al., 2023) but also modulate the energy budget balance of the Earth-atmosphere system (Bi et al., 2014, 2017; Che et al., 2024; Li et al., 2022), modify the microphysical properties of cloud droplets through complex semidirect and indirect effects of aerosols, and ultimately exert a profound impact on the global precipitation pattern and the hydrological cycle process (J. Huang et al., 2006, 2014; Li, Lau, et al., 2016; Rosenfeld et al., 2008). Last but not least, when dust particles are deposited on the surface of snow and ice by transregional transport, they would accelerate the melting of glaciers on Pamir Plateau by reducing the surface albedo of snow and ice sheets (Huang et al., 2011; Kang et al., 2019; Qian et al., 2014), and remarkably affect the supply of freshwater resources of Amu Darya and Syr Darya in Central Asia (Kayumov & Novikov, 2014). In September 1989, scientists from the former Soviet Union and the United States jointly initiated an intensive field campaign in southwest of Tadzhik U.S.S.R. during strong dust events for probing into the Central Asian desert dust and its effects of local meteorological processes and climate (Golitsyn & Gillette, 1993). The dust experiment has

investigated the source, transport, and deposition (Gillette et al., 1993); optical and microphysical-chemical properties of Central Asian desert aerosols (Andronova et al., 1993; Panchenko et al., 1993; Sviridenkov et al., 1993); and their direct radiative forcing (Sokolik & Golitsyn, 1993), as well as the impact on local meteorological conditions (Smirnov et al., 1993) in the Kafirnigan River Valley corridor (Ayvaj-Shaartuz-Esanbay-Dushanbe). Afterward, Abdullaev et al. (2014, 2019) studied the multiyear variations of AOD and  $AE_{440-870\text{ nm}}$  at Dushanbe—an AERONET site, and Bi et al. (2016) uncovered that pure dust aerosols at Dushanbe had weaker light absorption ability for wavelengths greater than 550 nm ( $SSA \sim 0.96-0.99$ ), but a moderate absorption in blue spectral wavelengths ( $SSA_{440\text{ nm}} \sim 0.92-0.93$ ). Hofer et al. (2017, 2020) surveyed the vertical profiles of mineral dust and polluted aerosols' optical features at Dushanbe based on 18-month measurements of a multiwavelength polarization Raman lidar. Rupakheti et al. (2020) assessed the seasonal variations of aerosol radiative forcing at Dushanbe based on AERONET retrieval products. Nonetheless, the aforementioned research studies were mainly devoted to inquiring the daytime aerosol optical and radiative properties at Dushanbe, and there is very lack to examine nighttime aerosol optical parameters, especially in desert source regions of southwest Tajikistan.

To this end, the Semi-Arid Climate and Environment Observatory of Lanzhou University (SACOL) and Physical-Technical Institute, Academy of Sciences of Republic of Tajikistan jointly established a permanent superobservatory—Ayvaj—in southwest of Tajikistan since 8 June 2023. The principal scientific objective of Ayvaj is to provide an unprecedented data sets of vertical profiles of dust aerosol optical and microphysical properties, air temperature, and water vapor density in Central Asia, and to completely ascertain the source, transregional transport, and deposition of dust particles, and their potential impacts on energy radiation budget, cloud microphysics, hydrological cycle, and ecological environment. A suite of state-of-the-art instruments were newly purchased and deployed at the Ayvaj site for carrying out long-term and continuous observations, such as, a multiwavelength Raman and polarization lidar (MRPL), a microwave profiler of air temperature and relative humidity (MWP967KV), a sun-sky-lunar photometer (CE318-T), a Grimm particle sizer spectrometer (EDM180), an aerosol particulate mass monitor (8533EP), surface net radiation fluxes (CNR4), soil parameter sensors, and automatic meteorological elements sensors. This study primarily investigates the diurnal and nocturnal behaviors of dust aerosol optical characteristics and explores their differences and similarities between daytime and nighttime at Ayvaj from June to October 2023 determined from sun-sky-lunar photometric measurements. The main structure of this article is as follows. Section 2 introduces the site information and instrumentation. Section 3 describes the calculation methods of daytime and nocturnal aerosol optical parameters. The major results analysis and discussion are illustrated in Section 4. And the primary conclusions are given in Section 5.

## 2. Site and Instrumentation

### 2.1. Site Information

The Shaartuz National Observatory—Ayvaj—(36.980°N, 68.023°E, 339 m above m.s.l.) is situated at the southernmost part of Kafirnigan River Valley in southwestern Tajikistan, and is about 160 km south of Dushanbe. The Ayvaj site is located on the border of Tajikistan, Uzbekistan, and Afghanistan (Amu Darya River), with Termez to the northwest (~70 km, Termez in Uzbekistan) and Balkh to the south (~35 km, Balkh in Afghanistan), which is a key intrusive passage for dust storms or mesoscale cold front systems from Afghanistan or West Asia to Dushanbe (Gillette et al., 1993; Smirnov et al., 1993). The village of Ayvaj has a total population of 6,500 and is dominated by primitive agricultural farming without any heavy industries or factories nearby. Therefore, the dust events originated from Ayvaj are virtually free from anthropogenic contamination. The climate pattern belongs to the typical continental arid and semidesert climate zone, and has four evident seasons, with hot and dry in summer, and cold and wet in winter. The annual mean temperature is about 17.1°C, from the coldest of -3.3°C in January to the hottest of 38.7°C in July, with an extremely significant diurnal and annual temperature difference. The annual average precipitation is about 100 ~ 223 mm, approximately 90% of which mainly concentrates in winter and spring seasons, while the evaporation is as high as 2,600 ~ 3,500 mm. The terrain of Ayvaj area is characterized by typical valley basin and coppice dunes with dry swales and rolling hillocks, and the desert-like vegetation is primarily covered with shrub steppe and perennial forbs, irrigated by freshwater from Kafirnigan River (Golitsyn & Gillette, 1993). On account of its unique topography and eco-environmental situations, the Ayvaj region is usually affected by frequent invasion of dust storms during dry seasons, and the elevated dust

particles are traveled straightly along the Kafirnigan River Valley to Dushanbe (Abdullaev & Sokolik, 2019; Golitsyn and Gillette, 1989; Sokolik & Golitsyn, 1993).

## 2.2. Sun-Sky-Lunar Photometer Measurements

A sun-sky-lunar multispectral photometer (model CE318-T), manufactured by the French *Cimel Electronique* since 2017, has been greatly updated for its operational functionalities and markedly improved the robust sun/moon tracking accuracy ( $<0.003^\circ$  resolution) with a new microstepping technique. Based on the normal CE318-N sun-sky photometer, the sensor head of the CE318-T is added to a new four-quadrant photodetector and a new signal amplifier with a signal-to-noise ratio better than 60 dB. The newly modified silicon photodiode detector (340–1,020 nm) and the InGaAs detector (1,020 and 1,640 nm) of CE318-T have a higher optical sensitivity and enhance the received photoelectric signal to be extended from  $0-2^{16}$  to  $0-2^{21}$ , performing a precise observation of lunar irradiances under a moon's illumination larger than 50% (Bi et al., 2024). The CE318-T photometer can automatically measure direct solar irradiances at spectral ranges of 340–1,640 nm during daytime and observe lunar irradiances at 440, 500, 675, 870, 936, 1,020, and 1,640 nm during nighttime, with a full-angle field of view (FOV) of  $1.26^\circ$  (Barreto et al., 2019). These solar/lunar photometric measurements can be utilized to compute multispectral aerosol optical depths, whereas the photoelectric signal at 936 nm is calculated columnar water vapor content in centimeter. The CE318-T can successively perform a consecutive sequence of triplet measurements of direct solar or moon's irradiances at each wavelength within one minute, which are used to efficiently distinguish and exclude cloud contamination data points as well as inspect the instrument's stability (Barreto et al., 2016, 2019; Giles et al., 2019). Meanwhile, the CE318-T can also take the different angular sky diffuse radiance scans in an almucantar and solar principal plane geometry for intensity and polarization measurements every 15 min, which could be applied to simultaneously retrieve aerosol volume size distribution, single-scattering albedo (SSA), complex refractive indices, and asymmetry factor (Lopatin et al., 2021; Torres et al., 2017). Note that the multispectral sky diffuse radiances at solar aureole and nocturnal lunar irradiances are measured with the same photodiode detector of direct solar irradiance, but with an electronic amplification factor and gain of 128 and 4,096, respectively.

## 2.3. Raman-Polarization Lidar System

A Multiwavelength Raman and Polarization Lidar (model MRPL) developed by Lanzhou University, China, is a highly integrated equipment for synchronously providing the vertical profiles of water vapor density within 3-km height and an aerosol extinction coefficient and depolarization ratio within 15 km (Dong et al., 2022; Zhang et al., 2022). The lidar emits three pulse laser beams at standard channels of 355, 532 and 1,064 nm into the atmosphere after laser collimation and beam expansion, and receives the attenuated backscattering signals from aerosol particles and a water vapor molecule with a 3.75-m vertical resolution and a 3-min time resolution. The emitted pulse energies (Nd:YAG, Q-switched) at diverse wavelengths vary from 80 to 200 mJ. The attenuated backscattering and orthogonal direction signal intensities at 532 nm could be used to retrieve the vertical structures of the aerosol extinction coefficient and the volumetric depolarization ratio. In addition, the vibrational Raman signals at 387 and 607 nm are utilized to determine water vapor density profiles during nighttime. A detailed description of MRPL's key specification is referred to Dong et al. (2022) and Zhang et al. (2022). In this study, we make use of the attenuated backscattering coefficient profiles detected from a lidar to validate the daytime and nocturnal AOD values from a collocated CE318-T photometer at Ayvaj.

## 2.4. Grimm Sizer Spectrometer Measurements

A Grimm particle sizer spectrometer (model EDM180, GRIMM Co., Germany) is designed to continuously measure aerosol size distribution and mass concentration with aerodynamic diameters from 0.25 to 32  $\mu\text{m}$  (31 channels) based on a light scattering principle of individual particles in the sampled air (Grimm & Eatough, 2009). The sample flow rate is set at 1.2 L/min, with flow error of  $<5\%$ . The measurement ranges of the particle number and mass concentrations are normally  $1 \sim 2 \times 10^6$  p/L and  $0.1 \sim 10$  mg/m<sup>3</sup>, respectively. An automatic constant temperature Nafion dryer system at the sampling inlet is used for dehumidification, but retaining the nonvolatile and semivolatile organic compounds of total particulate matters (i.e., PM<sub>1.0</sub>, PM<sub>2.5</sub> and PM<sub>10</sub>). Furthermore, an aerosol diluter (model 1.159, GRIMM Co.) is operated in series with an EDM180 spectrometer to dilute high-concentration aerosols (e.g., strong dust events or heavy haze episodes) with two adjusted dilution ratios of

1:1,000 and 1:10,000, which does not affect the particle size distribution measurements. All aerosol concentration data sets are automatically stored on a fixed computer with a 5-min average time resolution.

### 3. Methodology

#### 3.1. Calculation of Aerosol Optical Depth

The output digital voltage ( $V_j$ ) of the photometer is proportional to incoming monochromatic direct solar or lunar irradiance  $I_j$  ( $\text{W}/\text{m}^2/\text{nm}$ ) at the surface. According to Bouguer-Lambert-Beer law, the daytime and nocturnal aerosol optical depth ( $\tau_{a,j}$ ) can be calculated as follows (Ma et al., 2024):

$$\tau_{a,j} = \begin{cases} 1/m(\theta) \cdot \ln(V_{0,j,\text{Sun}}/V_{j,\text{Sun}}) - \tau_{R,j} - \tau_{g,j}, & \text{Sun,} \\ 1/m(\theta) \cdot \ln\left(\frac{A_j \times \Omega_M \times I_{0,j,\text{Sun}}}{\pi \times V_{j,\text{Moon}}}\right) \times \kappa_{j,\text{Moon}} \times RCF_j - \tau_{R,j} - \tau_{g,j}, & \text{Moon.} \end{cases} \quad (1)$$

Here,  $\tau_j$  is the total extinction optical depth (TOD) of various atmospheric constituents at wavelength  $j$ , the subscripts of  $a$ ,  $R$ , and  $g$  of  $\tau_j$  indicate the aerosol optical depth ( $\tau_{a,j}$ ), Rayleigh scattering of air molecules, and the absorption optical depth of diverse gases (i.e.,  $\text{O}_3$  and  $\text{NO}_2$ ), respectively.  $m(\theta)$  is relative air optical mass that is the inverse of cosine function of the solar or moon's zenith angle  $\theta$  (in radian) and computed by the observational geometry and time with a high precision.  $V_{j,\text{Sun}}$  and  $V_{j,\text{Moon}}$  are the output digital voltages of solar or lunar irradiances measured by a CE318-T photometer, respectively. The solar calibration coefficients ( $V_{0,j,\text{Sun}}$ ) were newly supplied by the French *Cimel Electronique* manufacturer, which were implemented by transfer calibration technology with a master reference photometer in a laboratory.

By contrast, the extraterrestrial voltages of spectral lunar irradiances at TOA ( $V_{0,j,\text{Moon}}$ ) dramatically vary with moon's phase angle (MPA), lunar libration, and the variations of reflectance characteristics of moon's surface even in one single night, attributed to the changing position of Moon, Sun, and Earth. Therefore,  $V_{0,j,\text{Moon}}$  were calculated by the product of lunar disk-equivalent reflectance ( $A_j$ ), Moon's solid angle ( $\Omega_M$ ), extraterrestrial solar irradiance ( $I_{0,j,\text{Sun}}$ ), and Moon calibration coefficients ( $\kappa_{j,\text{Moon}}$ ) (Barreto et al., 2016, 2019; Bi et al., 2024).  $A_j$  and  $\Omega_M$  were determined from the ROLO model (Kieffer & Stone, 2005), and  $I_{0,j,\text{Sun}}$  was computed from the convolution of spectral solar irradiances at TOA (Wehrli, 1986) and the filter transmittance function of a photometer. Many recent publications (Barreto et al., 2016, 2017, 2019; Bi et al., 2024; Uchiyama et al., 2019) have confirmed that the ROLO model could markedly underestimate the extraterrestrial lunar irradiances, which would result in invalid negative values of nocturnal AOD and a distinct cycle variation with MPA. To solve this problem, Román et al. (2020) proposed a method to improve the ROLO model with a correction factor ( $RCF_j$ ) to recalculate a new extraterrestrial lunar irradiance. Here, we take advantage of the RCF method recommended by Román et al. (2020) to redetermine the extraterrestrial lunar irradiance and nocturnal AODs at Ayvaj, which could effectively compensate the underestimated extraterrestrial lunar irradiances of the ROLO model for about 6.76%–9.78% (Bi et al., 2024). The RCF values are proved to vary with MPAs and wavelengths in a range from 1.01 to 1.14. As long as the solar or Moon calibration coefficient at a certain wavelength is determined, the daytime and nocturnal AOD values could be easily available according to Equation 1.

#### 3.2. Lunar-Langley Calibration Method

In this study, the Moon calibration coefficients ( $\kappa_{j,\text{Moon}}$ ) of the CE318-T photometer are deduced from lunar-Langley calibration method, which can be expressed as

$$\ln\left(\frac{V_{j,\text{Moon}}}{I_{0,j,\text{Moon}}}\right) = \ln(\kappa_{j,\text{Moon}}) - m(\theta) \times \tau_j \quad (2)$$

where  $V_{j,\text{Moon}}$  is the output digital voltage of lunar irradiances measured by a ground-based photometer, and  $I_{0,j,\text{Moon}}$  and  $m(\theta)$  are calculated from the ROLO-RCF model. Therefore, we can determine  $\kappa_{j,\text{Moon}}$  by implementing a least square fitting for  $\ln\left(\frac{V_{j,\text{Moon}}}{I_{0,j,\text{Moon}}}\right)$  versus  $m(\theta)$  under pristine, clear-sky, and stable atmospheric conditions. The intercept of the  $Y$ -axis is  $\ln(\kappa_{j,\text{Moon}})$  and the corresponding negative slope is total extinction optical

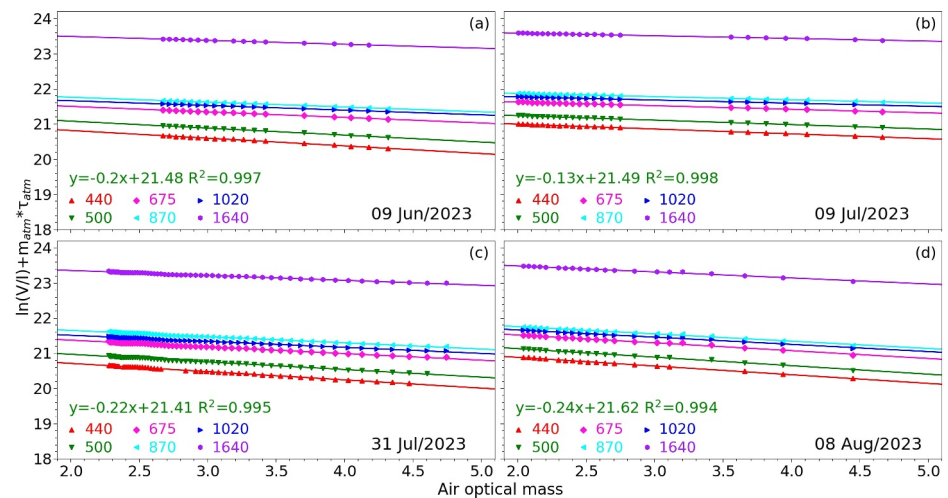


**Figure 1.** The lunar-Langley plot results with the ROLO model of Cimel#1627 performed at the Ayvadj site on (a) 9 June, (b) 9 July, (c) 31 July, and (d) 8 August 2023. The optimal least squares linear fitting equation and the correlation coefficient ( $R^2$ ) at 500-nm wavelength are shown in each figure. The subscript ‘*am*’ in the Y-axis indicates the Rayleigh scattering optical depth of air molecules.

depth ( $\tau_j$ ). This is the so-called classical lunar-Langley plot technique, which is widely used in inferring Moon calibration coefficients of a lunar photometer (Barreto et al., 2013, 2016, 2019; Bi et al., 2024; Z. Li, Li, et al., 2016).

Figure 1 depicts the lunar-Langley plot results with the ROLO-RCF model based on lunar irradiance measurements of a Cimel#1627 photometer at Ayvadj on 9th June, 9th July, 31st July, and 8th August, 2023. The optimal least squares linear fitting equation and the correlation coefficient ( $R^2$ ) at 500 nm are displayed in green color. The air optical mass of  $m(\theta)$  is chosen from 2.0 to 5.0 during moonrise or moonset. The selected four nighttime scenarios are clean, clear-sky and stable atmospheric conditions, with low background levels of aerosol loading and water vapor content (WVC). For instance, the AODs at 500 nm ( $AOD_{500\text{ nm}}$ ) retain relatively low and stable throughout the nighttime calibration period on July 9th and the mean  $AOD_{500\text{ nm}}$  and amplitude of variation are  $0.168 \pm 0.003\%$  and 3.8%, respectively. The corresponding WVC values vary from 1.38 to 1.44 cm during the moonrise or moonset on July 9th. The stable spectral lunar irradiances afford us a good opportunity to perform the Lunar-Langley plot to determine moon calibration coefficients. The results indicate that the optimal linear fits at six wave bands all exhibit a very excellent correlation relationship ( $R^2 \geq 0.990$ ), suggesting the reliability and robustness of the calibration technique. Figure 1 implies that the  $R^2$  at 500 nm are better than 0.994 for four cases. We eliminate those fitting data points with  $R^2$  less than 0.960 for each wavelength. After a rigorous inspection of obtained spectral moon calibration coefficients, we separately determine an optimal value of  $\kappa_{j,\text{Moon}}$  for each wavelength during the whole period. Finally, we can calculate accurately nocturnal AOD values at the spectral range of 440–1,640 nm according to Equation 1.

### 3.3. Spectral Deconvolution Algorithm (SDA)

The Ångström wavelength exponent ( $\alpha$ ) is designated as the slope of the logarithm of  $\tau_{a,j}$  versus the logarithm of wavelength, which is ordinarily used to represent the spectral dependence of  $\tau_{a,j}$  and to provide a qualitative indicator of aerosol particle size. For instance, a large value of  $\alpha$  ( $\sim 2.0$ ) stands for fine-mode small particles (i.e., urban haze or soot aerosol), while a small  $\alpha$  ( $\sim 0.5$ ) corresponds to coarse-mode large particles (i.e., dust or sea salt aerosol) (Dubovik et al., 2002; Schuster et al., 2006). In this study, we make use of a log linear fitting based on four wavelengths at 440, 500, 675, and 870 nm to compute  $\alpha$  according to the formula of  $\ln(\tau_{a,j}) = \ln(\beta) - \alpha \cdot \ln(j)$ . A spectral deconvolution algorithm (SDA) is utilized to extract the components of fine- and coarse-mode optical depths at 500 nm from the spectral total extinction AOD values (O’Neill et al., 2001, 2003). The SDA method is primarily based on two fundamental assumptions. The first is that the aerosol particle size distribution (PSD) is an effectively bimodal pattern. The second hypothesis is that the coarse-mode Ångström exponent and its spectral variations are both approximately neutral. The Ångström exponent  $\alpha$

and its second derivative ( $\alpha' = d\alpha/d \ln \lambda$ ) are the key input quantities of SDA procedure. These continuous function derivatives (computed at a reference wavelength of 500 nm) are acquired from a second-order polynomial fit of  $\ln \tau_a$  versus  $\ln \lambda$ . The spectral AOD values used as input to SDA are limited to six nominal wavelengths at 380, 440, 500, 675, 870, and 1,020 nm.

### 3.4. Cloud Screening Algorithm

The presence of clouds is the most important factor affecting the acquisition of accurate spectral AOD data. To acquire high-quality aerosol optical parameters at nighttime, it is very vital to reasonably exclude cloud influence data from clear-sky AOD data. In this paper, we apply a rigorous cloud screening algorithm and data quality procedure to eliminate the cloud contamination data (Barreto et al., 2019; Giles et al., 2019; Pérez-Ramírez et al., 2012). The basic principle is that temporal variations of clouds are significantly larger than those of aerosol particles. Consequently, diurnal stability check, smoothness criteria, and three standard deviation criteria are successively utilized in cloud screening procedure. In addition, a stability criterion of CE318-T triplet measurements within one minute are also used to set an empirical threshold of 0.015 in normalizing the range of these consecutive triplet values (i.e., the difference between maximum and minimum, divided by the mean value of triplets) (Bi et al., 2024).

## 4. Results Analysis and Discussion

### 4.1. Diurnal Cycles of Aerosol Optical Properties

Figure 2 shows the diurnal cycles of instantaneous multispectral AOD and  $AE_{440-870 \text{ nm}}$  derived from a Cimel#1627 photometer at Ayvay from 30 June to 31 October 2023. The gray backdrop denotes the nighttime measurements in a wide range of Moon's illumination and phase cycles. It indicates that the sun-sky-lunar photometer can reasonably observe the daytime and nocturnal aerosol optical parameters regardless of different levels of aerosol loadings. The spectral behaviors of AOD at various wavelengths exhibit consistent diurnal cycles, and nighttime AOD values also present a good continuity with daytime AODs in several consecutive days under different Moon illuminations. The airborne aerosol optical parameters at Ayvay in summer and autumn seasons of 2023 are significantly affected by the incursions of dust episodes. For example, a heavy dust event occurred at Ayvay on 31st August 2023, with the onset of 00:00 on 31st August and ending time of 04:00 on 1st September. The  $AOD_{500 \text{ nm}}$  increases sharply from 0.34 at 16:00 on 30th August to a maximum of 2.07 at 14:20 on 31st August, whereas the corresponding  $AE_{440-870 \text{ nm}}$  decreases dramatically from 0.73 to 0.18, suggesting that coarse-mode dust particles are dominant. Figure 2b presents a prominent feature that almost all  $AOD_{500 \text{ nm}}$  values are greater than 0.30 and  $AE_{440-870 \text{ nm}}$  values are smaller than 0.50 from 30th July to 2nd August, further substantiating the dominance of large dust particles.

Figure 3 outlines the time evolution of vertical profile of attenuated backscatter coefficient at 532 nm ( $\text{km}^{-1}\text{sr}^{-1}$ ) observed from lidar at Ayvay, and concurrent diurnal spectral AOD values and  $AE_{440-870 \text{ nm}}$  derived from Cimel#1627 photometer versus Moon's Phase Angle (MPA in  $^\circ$ ) from 28 August to 5 September 2023. The black solid line represents the variations of MPA during one complete full moon cycle. In order to more clearly characterize the different phases of the moon, the MPA was normalized by the actual moon's phase angle minus  $180^\circ$  in this study. Specifically, the negative MPA values represent the moonrise periods and positive MPA values represent the moonset periods, and  $MPA = 0^\circ$  corresponds to the full moon phase. A strong dust layer on 31st August is perfectly captured using a lidar, and the peak values of attenuated signals concentrate on 0.0–0.5 km height with the strongest backscattering coefficient of  $1.13 \times 10^{-2} \text{ km}^{-1}\text{sr}^{-1}$ . The  $AOD_{500 \text{ nm}}$  values are greater than 0.80, and corresponding  $AE_{440-870 \text{ nm}}$  are less than 0.40 during the invasion of dust event. A high-concentration level ( $0.3 \sim 0.6 \times 10^{-2} \text{ km}^{-1}\text{sr}^{-1}$ ) of aerosol particle layer persistently hangs over at 1.0–3.5-km height from 1st to 3rd September, primarily due to the influence of dust storm transport in surrounding region. Additionally, several evident cloud layers at the 4.0–7.0-km altitude are distinctly detected using a lidar, appearing on 28th and 31st August and 4th September 2023, respectively. These cloud contamination data sets are efficiently distinguished and eliminated by the cloud screening algorithm for AOD values of the CE318-T photometer, which provides well-documented evidence that the cloud identification method used in this study is reliable and robust. Figure 3b shows that spectral AOD values and  $AE_{440-870 \text{ nm}}$  present a noticeable diurnal change during the period. And large AOD values of the photometer generally correspond well to the high levels of the backscattering coefficient observed using a lidar. Both multispectral AODs and  $AE_{440-870 \text{ nm}}$  exhibit an

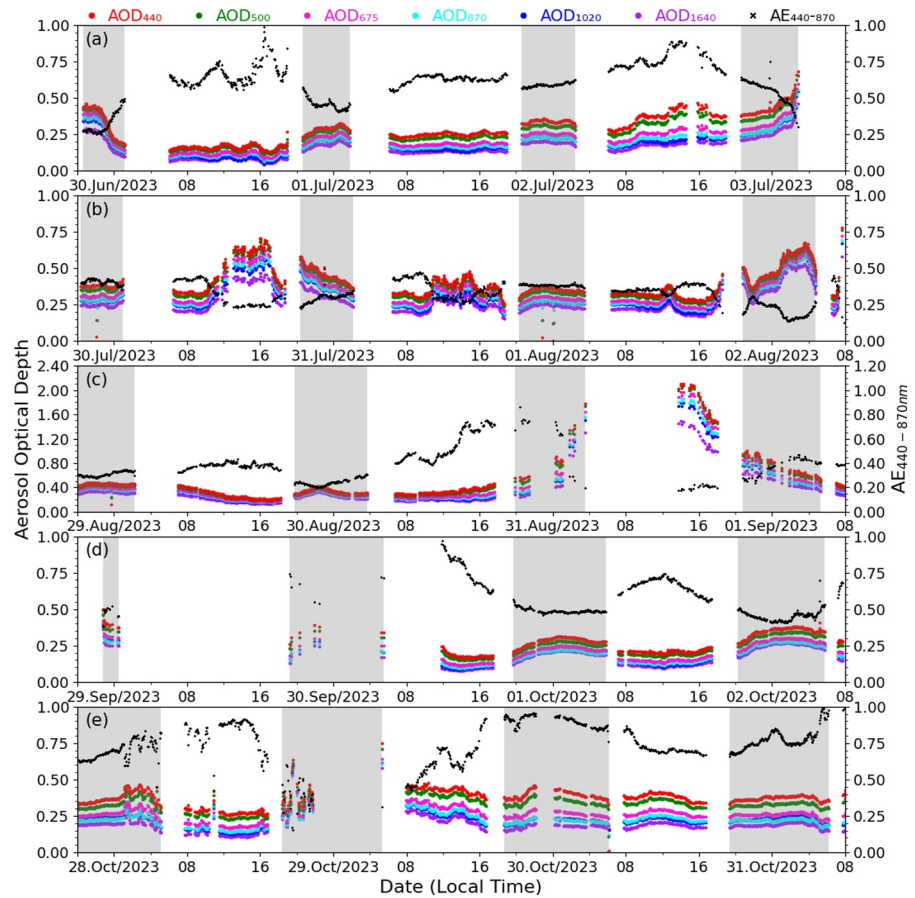


**Figure 2.** Diurnal cycles of multispectral aerosol optical depth (AOD, X-axis) and Ångström exponent ( $AE_{440-870\text{ nm}}$ , Y-axis) derived from Cimel#1627 photometer at Ayvaj from 30 June to 31 October 2023. The gray backdrop denotes the nighttime measurements. Different colors solid circles denote AOD at various wavelengths, and x denotes  $AE_{440-870\text{ nm}}$ . (a) is from 30 June to 3 July 2023, (b) is from 30 July to 2 August 2023, (c) is from 29 August to 1 September 2023, (d) is from 29 September to 2 October 2023 and (e) is from 28 to 31 October 2023.

excellent continuity of diurnal variation from daytime to nighttime, and are not distinctly dependent on MPA. The aerosol optical properties at Ayvaj are significantly affected by the intrusions of dust events. For instance, the  $AOD_{500\text{ nm}}$  values vary from 0.20 to 0.30 and  $AE_{440-870\text{ nm}}$  are larger than 0.60 under a nondusty event (i.e., 3rd September), whereas all  $AOD_{500\text{ nm}}$  are greater than 0.40 and  $AE_{440-870\text{ nm}}$  are smaller than 0.50 under dust episodes (i.e., 31st August, 1–3 September). This indicates that high aerosol loading and coarse-mode dust particles are predominant in Ayvaj from 31st August to 3rd September.

#### 4.2. AOD Day/Night Transition Coherence Test

In order to verify the reliability of AODs obtained from a CE318-T photometer at night-to-day and day-to-night time intervals, Barreto et al. (2016) first proposed the AOD day/night transition coherence test method by quantitatively analyzing the AOD differences between daytime and nighttime measurements using a photometer. As recommended by Barreto et al. (2016), we calculate mean values of AODs in the last 1 hr of daytime data ( $AOD_{\text{sunset}}$ ) and the corresponding values in the first 1 hr of nocturnal data ( $AOD_{\text{moonrise}}$ ) under different Moon phase cycles. Subsequently, we also compute the average values of AODs in the first 1 hr of daytime data ( $AOD_{\text{sunrise}}$ ) and the last 1 hr of nighttime data ( $AOD_{\text{moonset}}$ ) at Ayvaj during the same period. In this section, we perform the AOD day/night transition coherence test by considering AOD measurements under relatively stable changes of aerosol loading within a few hours. We also require average time differences  $\leq 3$  hr between AOD measurements observed at night-to-day and day-to-night time intervals (Barreto et al., 2016; Perrone et al., 2022). There are 17 cases of  $AOD_{\text{moonrise}}$  and  $AOD_{\text{sunset}}$  pairwise values, and 14 cases of  $AOD_{\text{moonset}}$  and  $AOD_{\text{sunrise}}$

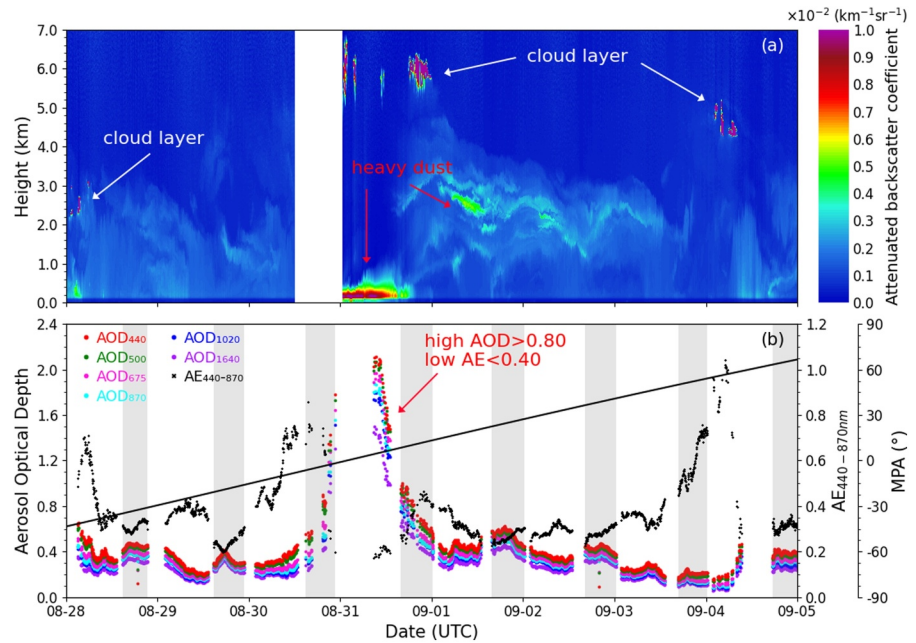


**Figure 3.** Time evolution of (a) vertical profile of the attenuated backscatter coefficient at 532 nm (in  $\text{km}^{-1}\text{sr}^{-1}$ ) observed using a lidar and (b) concurrent spectral AOD and  $\text{AE}_{440-870\text{nm}}$  derived using a Cimel#1627 photometer versus Moon's phase angle (MPA in  $^\circ$ ) from 28 August to 5 September 2023. The white blank period in Figure 3a represents the failure of lidar observations due to power supply outages. The gray backdrop denotes the nighttime measurements using a photometer. The black solid line shows the variations of MPA during one complete full moon cycle.

**Table 1**

Summary Statistics of Mean AOD at 500 nm in the Last 1 hr of Daytime Data ( $\text{AOD}_{\text{sunset}}$ ) and the Corresponding Values in the First 1 hr of Nocturnal Data ( $\text{AOD}_{\text{moonrise}}$ ) at Ayvay Site From June to October 2023

Date of 2023	Last 1 hr of $\text{AOD}_{\text{sunset}}$			First 1 hr of $\text{AOD}_{\text{moonrise}}$			Differ. $\Delta\text{AOD}_{\text{MR}}$
	Start	End	Mean $\pm$ Std	Start	End	Mean $\pm$ Std	
06–29	17:58:06	18:58:06	0.417 $\pm$ 0.025	20:36:48	21:36:48	0.424 $\pm$ 0.025	0.007
07–02	17:53:15	18:53:15	0.334 $\pm$ 0.005	20:36:47	21:36:47	0.347 $\pm$ 0.005	0.013
07–29	17:39:50	18:39:50	0.344 $\pm$ 0.014	20:21:47	21:21:47	0.353 $\pm$ 0.014	0.009
07–31	17:42:54	18:42:54	0.304 $\pm$ 0.048	20:21:47	21:21:47	0.304 $\pm$ 0.048	0.0
08–01	17:31:49	18:31:49	0.351 $\pm$ 0.041	20:45:47	21:45:47	0.423 $\pm$ 0.041	0.072
08–26	17:19:45	18:19:45	0.368 $\pm$ 0.007	19:48:47	20:48:47	0.359 $\pm$ 0.007	–0.009
08–30	16:37:55	17:37:55	0.389 $\pm$ 0.016	19:54:47	20:54:47	0.488 $\pm$ 0.016	0.099
09–01	16:55:08	17:55:08	0.437 $\pm$ 0.032	20:48:47	21:48:47	0.533 $\pm$ 0.032	0.096
09–22	16:36:48	17:36:48	0.227 $\pm$ 0.004	19:06:47	20:06:47	0.243 $\pm$ 0.004	0.016
09–23	16:32:23	17:32:23	0.211 $\pm$ 0.013	19:03:47	20:03:47	0.262 $\pm$ 0.013	0.051
09–25	16:32:13	17:32:13	0.207 $\pm$ 0.002	19:00:47	20:00:47	0.248 $\pm$ 0.002	0.041
09–30	16:26:58	17:26:58	0.160 $\pm$ 0.002	19:39:47	20:39:47	0.201 $\pm$ 0.002	0.041
10–01	16:23:33	17:23:33	0.213 $\pm$ 0.006	20:12:47	21:12:47	0.254 $\pm$ 0.006	0.041
10–24	15:44:51	16:44:51	0.268 $\pm$ 0.008	18:21:48	19:21:48	0.277 $\pm$ 0.008	0.009
10–27	15:39:34	16:39:34	0.271 $\pm$ 0.031	18:18:47	19:18:47	0.292 $\pm$ 0.031	0.021
10–29	15:41:45	16:41:45	0.342 $\pm$ 0.017	18:39:47	19:39:47	0.320 $\pm$ 0.017	–0.022
10–30	15:44:33	16:44:33	0.309 $\pm$ 0.003	19:18:47	20:18:47	0.316 $\pm$ 0.003	0.007

Note. The ' $\Delta\text{AOD}_{\text{MR}}$ ' denotes the difference between  $\text{AOD}_{\text{moonrise}}$  and  $\text{AOD}_{\text{sunset}}$ .

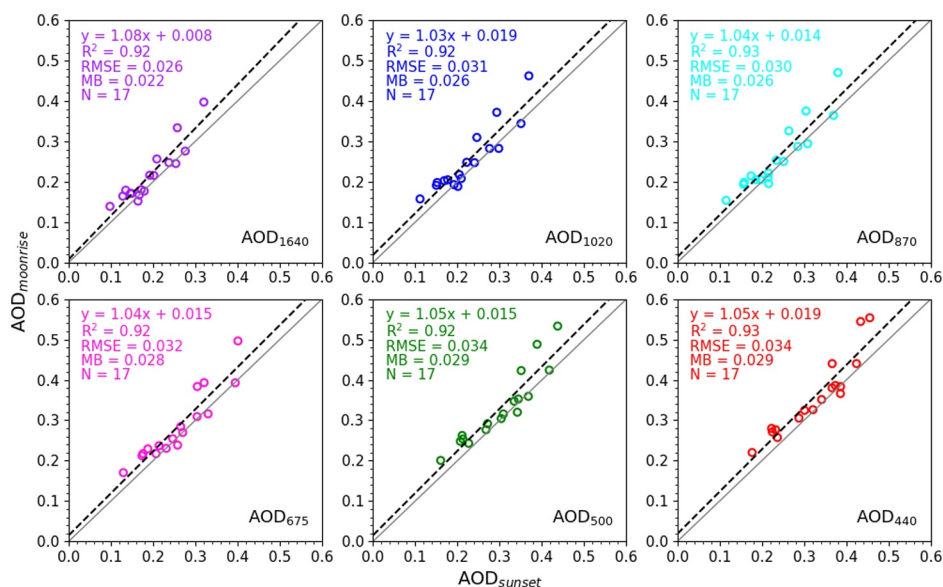
**Table 2**

The Same as Table 1, Except for Mean AOD at 500 nm in the First 1 hr of Daytime Data ( $AOD_{\text{sunrise}}$ ) and the Last 1 hr of Nighttime Data ( $AOD_{\text{moonset}}$ ) at Ayvaj

Date of 2023	Last 1 hr of $AOD_{\text{moonset}}$			First 1 hr of $AOD_{\text{sunrise}}$			Differ. $\Delta AOD_{\text{MS}}$
	Start	End	Mean $\pm$ Std	Start	End	Mean $\pm$ Std	
07–10	03:30:49	04:30:49	0.282 $\pm$ 0.004	06:09:33	07:09:33	0.230 $\pm$ 0.004	0.052
08–01	02:24:47	03:24:47	0.323 $\pm$ 0.005	06:24:48	07:24:48	0.309 $\pm$ 0.005	0.014
08–03	03:51:47	04:51:47	0.317 $\pm$ 0.014	06:30:41	07:30:41	0.221 $\pm$ 0.014	0.096
08–06	03:54:49	04:54:49	0.350 $\pm$ 0.003	06:27:26	07:27:26	0.248 $\pm$ 0.003	0.102
08–08	03:54:49	04:54:49	0.252 $\pm$ 0.004	06:30:15	07:30:15	0.267 $\pm$ 0.004	−0.015
08–09	03:57:49	04:57:49	0.190 $\pm$ 0.003	06:30:09	07:30:09	0.173 $\pm$ 0.003	0.017
09–01	04:18:47	05:18:47	0.524 $\pm$ 0.031	06:59:09	07:59:09	0.417 $\pm$ 0.031	0.107
09–02	04:18:48	05:18:48	0.432 $\pm$ 0.011	06:55:31	07:55:31	0.396 $\pm$ 0.011	0.036
09–06	04:24:50	05:24:50	0.265 $\pm$ 0.003	06:50:28	07:50:28	0.266 $\pm$ 0.003	−0.001
10–03	04:45:49	05:45:49	0.270 $\pm$ 0.010	07:11:58	08:11:58	0.212 $\pm$ 0.010	0.058
10–04	04:45:49	05:45:49	0.235 $\pm$ 0.047	07:34:35	08:34:35	0.279 $\pm$ 0.047	−0.044
10–28	04:09:47	05:09:47	0.318 $\pm$ 0.038	07:45:30	08:45:30	0.267 $\pm$ 0.038	0.051
10–30	05:09:48	06:09:48	0.309 $\pm$ 0.048	07:48:22	08:48:22	0.333 $\pm$ 0.048	−0.024
10–31	05:09:48	06:09:48	0.299 $\pm$ 0.007	07:45:19	08:45:19	0.360 $\pm$ 0.007	−0.061

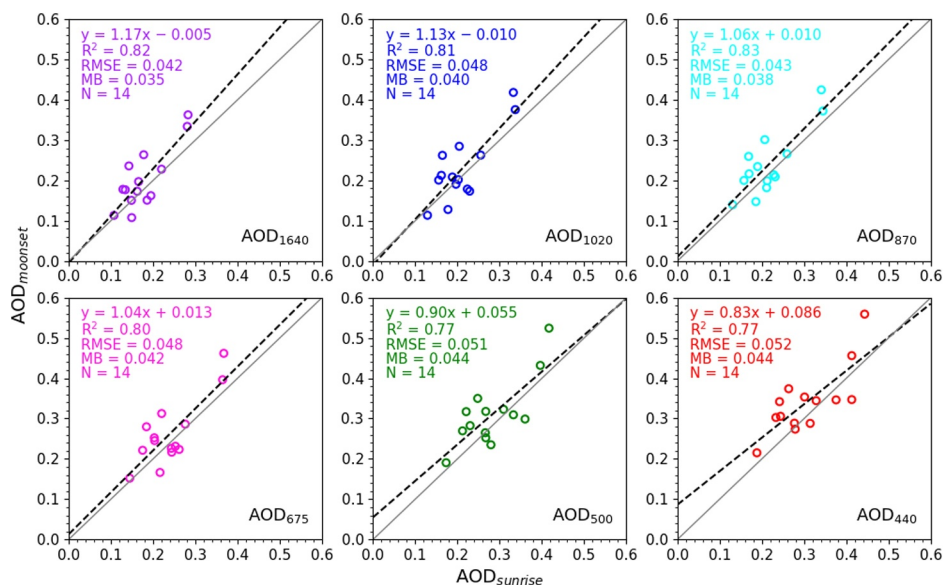
values for coherence test at Ayvaj during the whole period. Tables 1 and 2 summarize the statistical parameters of  $AOD_{\text{moonrise}}$  and  $AOD_{\text{sunset}}$  and  $AOD_{\text{moonset}}$  and  $AOD_{\text{sunrise}}$  values at 500 nm in Ayvaj, respectively. The ‘ $\Delta AOD_{\text{MR}}$ ’ denotes the difference between  $AOD_{\text{moonrise}}$  and  $AOD_{\text{sunset}}$  (before full moon), while ‘ $\Delta AOD_{\text{MS}}$ ’ represents the discrepancy between  $AOD_{\text{moonset}}$  and  $AOD_{\text{sunrise}}$  (after full moon). It is clear that  $AOD_{\text{moonrise}}$  and  $AOD_{\text{sunset}}$  values at 500 nm span the ranges of 0.201 ~ 0.533 and 0.160 ~ 0.437, respectively. Pairwise comparisons implemented by Gaussian distribution show that  $AOD_{\text{moonrise}}$  and  $AOD_{\text{sunset}}$  values are consistent variations at a 95% confidence level. The corresponding  $\Delta AOD_{\text{MR}}$  value increases distinctly with the increase of  $AOD_{\text{moonrise}}$ . For instance, the  $\Delta AOD_{\text{MR}}$  and  $AOD_{\text{moonrise}}$  values on 30th August and 1st September are 0.099 and 0.488  $\pm$  0.016, and 0.096 and 0.533  $\pm$  0.032, respectively, which is mainly ascribed to the impact of incursive dust events, as documented in Figure 3. Similarly,  $AOD_{\text{moonset}}$  and  $AOD_{\text{sunrise}}$  values span the ranges of 0.190 ~ 0.524 and 0.173 ~ 0.417, respectively, and the pairwise comparisons also display no significant difference at a 95% confidence level. If we do not consider the influences of dust events (e.g., 1st, 3rd, and 30th August and 1st September), the absolute differences of  $\Delta AOD_{\text{MR}}$  and  $\Delta AOD_{\text{MS}}$  at 500 nm vary at the ranges of (0.007 ~ 0.051) and (0.001 ~ 0.061), respectively, which are slightly greater but fall within the accuracy level of lunar AODs (Barreto et al., 2019; Bi et al., 2024) and solar AODs (Giles et al., 2019).

Figure 4 describes the scatterplots of  $AOD_{\text{moonrise}}$  and  $AOD_{\text{sunset}}$  values at diverse wavelengths from June to October 2023 at Ayvaj. The regression line (dashed) and 1:1 line (gray solid line) are shown in each plot, as well as  $R^2$ , root mean square error (RMSE), mean bias (MB), and total number of days for data points (N). It indicates that both the  $AOD_{\text{moonrise}}$  and  $AOD_{\text{sunset}}$  values exhibit an excellent agreement and  $R^2$ , and RMSE and MB are better than 0.92, less than 0.034 and 0.029 for all wavelengths, respectively. The linear fitting equation of  $AOD_{\text{moonrise}}$  and  $AOD_{\text{sunset}}$  values at 500 nm is  $y = 1.05x + 0.015$ , and the other channels also show similar fitting results. Figure 5 is the same as Figure 4, except for the scatterplots between  $AOD_{\text{moonset}}$  and  $AOD_{\text{sunrise}}$  values at Ayvaj. Likewise, the  $AOD_{\text{moonset}}$  and  $AOD_{\text{sunrise}}$  values at various wavelengths also present a good consistency, but are slightly worse than the former. For example, all the  $R^2$  values are greater than 0.77, and the MSE and MB are smaller than 0.052 and 0.044, respectively, which is likely affected by frequent dust events and a nighttime atmospheric inversion layer. The linear fitting equation of  $AOD_{\text{moonset}}$  and  $AOD_{\text{sunrise}}$  values at 500 nm is  $y = 0.90x + 0.055$ , as shown in Figure 5. These impressive results demonstrate the reliability of nocturnal AOD values acquired using a CE318-T photometer at night-to-day and day-to-night time intervals under stable aerosol loading cases.



**Figure 4.** Scatterplots of mean AODs in the last 1 hr of daytime data ( $AOD_{\text{sunset}}$ ) and the corresponding values in the first 1 hr of nocturnal data ( $AOD_{\text{moonrise}}$ ) from June to October 2023 at Ayvaj. The regression line (dashed) and 1:1 line (gray solid line) are shown in each plot, as well as correlation coefficient ( $R^2$ ), root mean square error (RMSE), mean bias (MB), and total number of days for data points (N).

Figure 6 delineates the scatterplots of mean  $AE_{440-870 \text{ nm}}$  in the last 1 hr of daytime  $AOD_{\text{sunset}}$  data versus the first 1 hr of nocturnal  $AOD_{\text{moonrise}}$  data and the corresponding values in the first 1 hr of diurnal data  $AOD_{\text{sunrise}}$  versus  $AOD_{\text{moonset}}$  from June to October 2023 at Ayvaj. Obviously, the  $AE_{440-870 \text{ nm}}$  values at the nocturnal  $AOD_{\text{moonrise}}$  period show a well consistent linear relationship with those at the daytime  $AOD_{\text{sunset}}$  period, and  $R^2$ , RMSE, and MB are 0.95, 0.056, and 0.048, respectively. The linear fitting equation at 500 nm is  $y = 0.90x + 0.056$ . From Figure 6b, the  $AE_{440-870 \text{ nm}}$  values between the  $AOD_{\text{moonset}}$  period and the  $AOD_{\text{sunrise}}$  period also reveal a good consistency, and  $R^2$ , RMSE, and MB are 0.93, 0.085, and 0.065, respectively. And the corresponding linear fitting equation at 500 nm is  $y = 0.97x - 0.012$ . The AOD day/night transition coherence test further corroborates that the



**Figure 5.** The same as Figure 4, but for the mean AODs in the first 1 hr of daytime data ( $AOD_{\text{sunrise}}$ ) and the last 1 hr of nighttime data ( $AOD_{\text{moonset}}$ ) at Ayvaj.

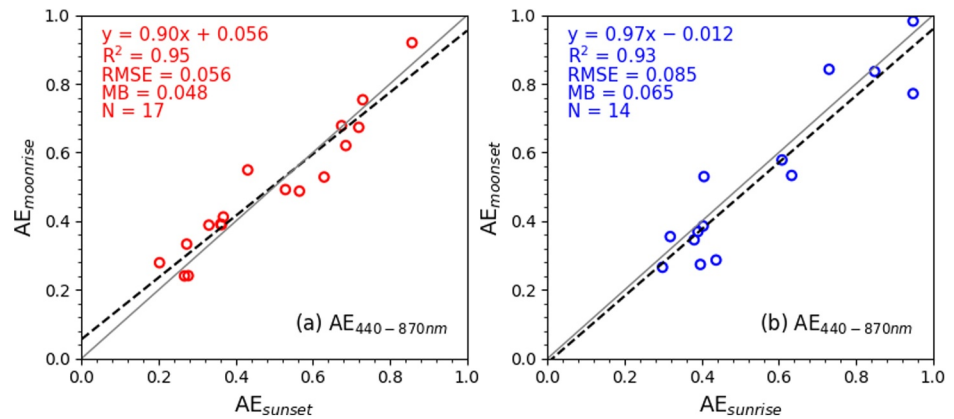


**Figure 6.** Scatterplots of mean  $AE_{440-870\text{ nm}}$  in the last 1 hr of daytime  $AE_{\text{sunset}}$  data versus the first 1 hr of nocturnal  $AE_{\text{moonrise}}$  data (left panel) and the corresponding values in the first 1 hr of diurnal data  $AE_{\text{sunrise}}$  versus  $AE_{\text{moonset}}$  (right panel) from June to October 2023 at Ayvaj.

nocturnal AODs at spectral range of 440–1,640 nm in Ayvaj derived using a CE318-T photometer are reliable and trustworthy during the whole period.

Note that there is a full moon phase cycle from 25 July to 9 August 2023 at Ayvaj (MPA:  $-90.0^\circ \sim 90.0^\circ$ ). Figure 7 draws the time series of nocturnal AODs at 440, 500, 870, and 1,020 nm and  $AE_{440-870\text{ nm}}$  versus Moon's illumination factor (MIF in %) at Ayvaj from 25 July to 9 August 2023. The daytime AOD values are also displayed with pink triangles. The black curve denotes the corresponding evolution of MIF >50% during the full moon period, which is usually utilized to represent the dependence of nocturnal AOD value on MPA. The nighttime AODs at the other wave bands also show similar diurnal variations, but are not shown here. It is evident that the nocturnal AOD values at diverse wavelengths measured using a CE318-T photometer exhibit a well consecutive variation with corresponding AOD values at daytime. Specifically, multispectral nocturnal AOD values at Ayvaj are not strikingly dependent on MIF or MPA, and show a reasonable diurnal continuity under different Moon illumination conditions and aerosol loading levels. There are not artificially negative values of nocturnal AOD at all wavelengths during the period, which once again supports the reliability of nighttime AODs at Ayvaj (Barreto et al., 2019; Bi et al., 2024). For instance, the nocturnal  $AOD_{500\text{ nm}}$  value is equal to 0.334 at 00:01 a.m. on 1st August (full moon, MIF = 98%), which is close to that of 0.330 at 18:13 p.m. on 31st July (i.e., last AOD before sunset). As another example, the nocturnal  $AOD_{500\text{ nm}}$  is equal to 0.250 at 00:04 a.m. on 8th August (last quarter of the moon, MIF = 57%), which is close to that of 0.257 at 07:09 a.m. on 8th August (i.e., first AOD after sunrise). It is worth noting that nighttime AOD values at 870 and 1,020 nm are slightly underestimated, especially under low MIF conditions (MIF < 65%) or high MPA scenarios (MPA > 50° or MPA < -50°), which is probably due to the ROLO lunar irradiance model and the instrument's calibration. For example, the nocturnal  $AOD_{870\text{ nm}}$  is equal to 0.196 at 20:28 p.m. on 25th July (i.e., first AOD after moonrise, MIF = 57%), which is less than that of 0.224 at 18:51 p.m. on 25th July (i.e., last AOD before sunset). And the nocturnal  $AOD_{870\text{ nm}}$  value is about 0.216 at 04:55 a.m. on 8th August (i.e., last AOD before moonset, MIF = 55%), which is lower than that of 0.250 at 06:31 a.m. on 8th August (i.e., first AOD after sunrise). The detailed reasons deserve to be further explored in the future. In consequence, the nocturnal  $AE_{440-870\text{ nm}}$  values generally present reasonable consecutive variations and are well consistent with the corresponding  $AE_{440-870\text{ nm}}$  at daytime, especially nearby the full moon phase (i.e., 1st August) and under high MIF ( $\geq 65\%$ ) cases. However, there are a few cases where nighttime  $AE_{440-870\text{ nm}}$  values are slightly overestimated under low Moon's illumination conditions. For instance, the nocturnal  $AE_{440-870\text{ nm}}$  is about 0.450 at 20:28 p.m. on 25th July (i.e., first AOD after moonrise, MIF = 57%), which is greater than that of 0.352 at 18:51 p.m. on 25th July (i.e., last AOD before sunset), majorly attributable to the underestimation of corresponding nighttime  $AOD_{870\text{ nm}}$  values.

### 4.3. Aerosol Characteristics Under Heavy Dust Events

In June 2023, four heavy dust events appeared at the Ayvaj region, such as the ones in 9–12, 19–20, 23, and 25–28 June. Among them, the dust episode that occurred from 9th to 12th June was the strongest intensity and longest time of duration one. Prior to the dust storm, the southwestern area of Tajikistan had experienced a prolonged

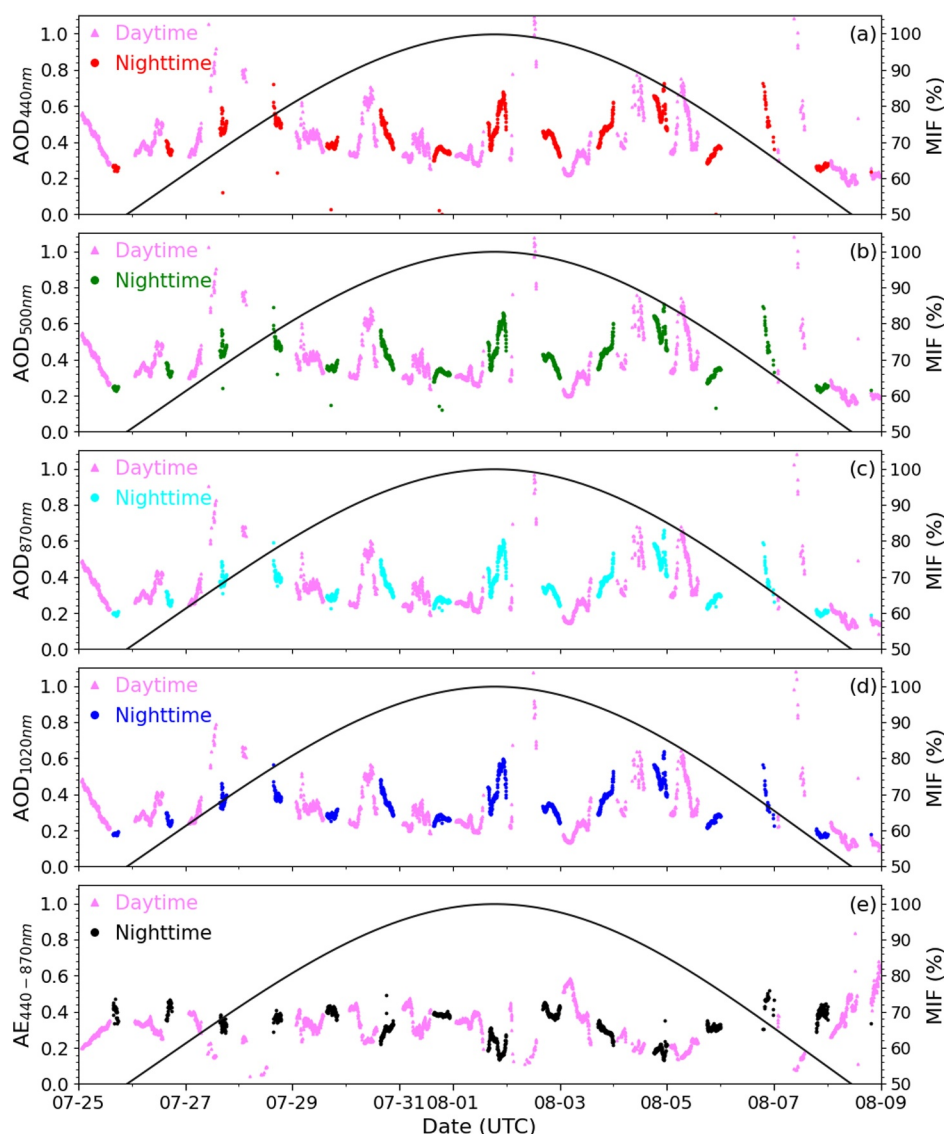


**Figure 7.** Time series of nocturnal AODs at (a) 440, (b) 500, (c) 870, and (d) 1020 nm and (e)  $AE_{440-870\text{ nm}}$  versus Moon's illumination factor (MIF in %) at Ayvaj from 25 July to 9 August 2023. The daytime AOD values are also displayed with pink triangles, which are computed from Bouguer-Lambert-Beer law. The nighttime AOD values are shown with different colors of solid circles. The black curve denotes the corresponding evolution of MIF >50% during the entire period. There is a full moon phase cycle from 25 July to 9 August 2023 at Ayvaj (MPA:  $-90.0^\circ \sim 90.0^\circ$ ).

period of clear skies, extreme heat waves, and drought without any precipitation. For example, the daily maximum air temperature on 6th June recorded at the national observatory—Ayvaj—was as high as  $43^\circ\text{C}$ , and the soil moisture at 10-cm depth was only  $0.002\text{ m}^3\text{m}^{-3}$ . The intense sunshine persistently heats the soil layer and the atmosphere, drying out the bare desert soil, which provided a favorable material basis for the formation of dust storm. Beginning at 08:00 a.m. on 9th June, an intense synoptic scale cold front cyclone passed through Ayvaj, accompanied by strong surface winds and could easily blow fine soil particles from the ground level into the upper air, triggering dust storm events. These dust processes, which occurred in June, were successfully detected by the advanced ground-based instruments at Ayvaj. Figure 8 illustrates the diurnal variations of spectral AOD values and  $AE_{440-870\text{ nm}}$  derived using a Cimel#1627 photometer at Ayvaj from 8 to 30 June 2023, and five-minute averaged surface  $PM_{1.0}$ ,  $PM_{2.5}$ , and  $PM_{10}$  mass concentrations in  $\text{mg}/\text{m}^3$  measured using a GRIMM sizer spectrometer. The overall average value and one standard deviation are in parentheses. Note that the GRIMM spectrometer was in continuous operation from 8 to 21 June, due to the instrument malfunction. It is evident that

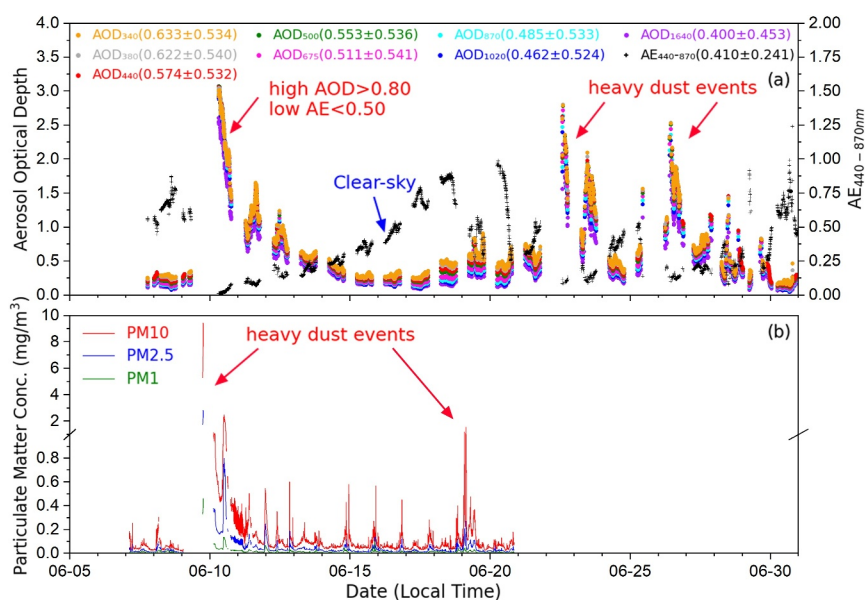


**Figure 8.** Diurnal variations of (a) spectral AOD and  $AE_{440-870\text{ nm}}$  derived using a Cimel#1627 photometer at Ayvay from 8 to 30 June 2023, (b) five-minute averaged surface  $PM_{1.0}$ ,  $PM_{2.5}$ , and  $PM_{10}$  mass concentrations (in  $\text{mg}/\text{m}^3$ ) measured using a GRIMM particle sizer spectrometer. The overall average value and one standard deviation are in parentheses. There were several heavy dust episodes during the period.

the aerosol optical properties at Ayvay show a prominent diurnal variation, with the total mean  $AOD_{500\text{ nm}}$  and  $AE_{440-870\text{ nm}}$  of  $0.553 \pm 0.536$  and  $0.410 \pm 0.241$ , respectively. The  $AOD_{500\text{ nm}}$  values change from 0.10 to 3.07, and  $AE_{440-870\text{ nm}}$  values vary from 0.01 to 1.24. The corresponding standard deviations of aerosol optical parameters are closely linked with the frequent dust episodes and display dramatic fluctuations. For instance, the  $AOD_{500\text{ nm}}$ ,  $AE_{440-870\text{ nm}}$ , and WVC values remain at ranges of  $0.16 \sim 0.30$ ,  $0.44 \sim 0.87$ , and  $1.05 \sim 1.37\text{ cm}$  under clear-sky and dust-free circumstances (i.e., 8th June), respectively, whereas the corresponding values are  $1.40 \sim 3.07$ ,  $0.01 \sim 0.08$ , and  $1.86 \sim 2.13\text{ cm}$  under heavy dust events (i.e., 10th June), which are greater than those in Dushanbe under the worst dust haze during the period 2010–2015 (with  $AOD_{500\text{ nm}}$  and  $AE_{440-870\text{ nm}}$  of 2.78 and 0.12; Abdullaev & Sokolik, 2019). This corroborates that the dust storms produce extremely high aerosol loadings and coarse large particles are dominant in the whole columnar atmosphere of Ayvay. Subsequently, the variation ranges of  $AOD_{500\text{ nm}}$ ,  $AE_{440-870\text{ nm}}$ , and WVC values are  $0.79 \sim 1.64$ ,  $0.07 \sim 0.13$ , and  $1.99 \sim 2.17\text{ cm}$  on 11th June, and are  $0.61 \sim 1.17$ ,  $0.13 \sim 0.22$ , and  $2.21 \sim 2.69\text{ cm}$  on 12th June, respectively. Although the multispectral AOD values decrease gradually with the weakening of dust intensities from 10th to 12th June, the  $AOD_{500\text{ nm}}$  values are always bigger than 0.60 and  $AE_{440-870\text{ nm}}$  are less than 0.25 during the entire dust events, suggesting that pure dust and coarse mineral particles are overwhelmingly predominant (Bi et al., 2016). This is to be expected, because the Ayvay region is virtually unaffected by human activities. Figure 8b indicates that the background levels of surface  $PM_{2.5}$  and  $PM_{10}$  mass concentrations keep stable at  $20 \sim 40$  and  $50 \sim 80\ \mu\text{g}/\text{m}^3$  from 7th to 8th June (i.e., nondusty days). However, the  $PM_{2.5}$  and  $PM_{10}$  concentrations increase sharply from 08:00 a.m. on 9th June and reach the maxima of  $2,000 \sim 2,820$  and  $8,000 \sim 9,440\ \mu\text{g}/\text{m}^3$  ( $1\text{ mg} = 1,000\ \mu\text{g}$ ) at 13:00 p.m. on 9th June, respectively, which are about 60 and 120 times, respectively, of the values specified by the World Health Organization Air Quality Guidelines of  $35$  and  $75\ \mu\text{g}/\text{m}^3$  for  $PM_{2.5}$  and  $PM_{10}$ , respectively (World Health Organization, 2005). The maximal  $PM_{10}$  concentration is even much larger than that of  $6,000\ \mu\text{g}/\text{m}^3$  in Shaartuz during a strong dust storm process on 20th September, 1989 (Sviridenkov et al., 1993). And  $PM_{2.5}$  and  $PM_{10}$  concentrations decrease gradually with the weakening of dust intensity, and are  $150 \sim 700$  and  $500 \sim 2,500\ \mu\text{g}/\text{m}^3$  on 10th June, and are  $50 \sim 220$  and  $100 \sim 550\ \mu\text{g}/\text{m}^3$  on 11th June, respectively. This unveils that the near-surface pollution of large dust particles are also unprecedentedly severe in June 2023 at Ayvay. Such high concentrations of ambient particulate matters undoubtedly exert a far-reaching impact on public health, diurnal exposure, air quality, and climate change on the regional scale.

As aforementioned, the Ångström exponent is an intensive optical quantity for characterizing the spectral dependence of AODs and is a good indicator of aerosol size distribution. Figure 9 displays the scatterplots of

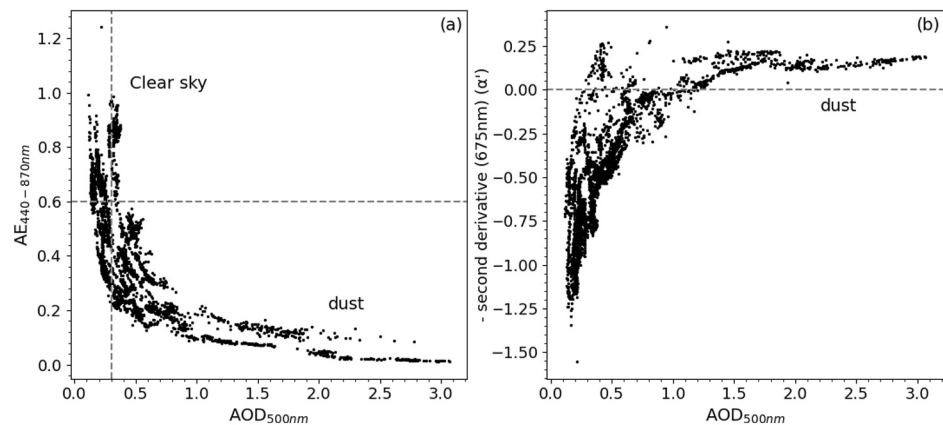


**Figure 9.** Scatterplots of instantaneous (a)  $AE_{440-870\text{ nm}}$  versus  $AOD_{500\text{ nm}}$  and (b) the negative of second derivative of  $\ln(AOD)$  with  $\ln(\alpha)$  versus  $AOD_{500\text{ nm}}$  acquired using a Cimel#1627 photometer at Ayvay from 8 to 30 June 2023.

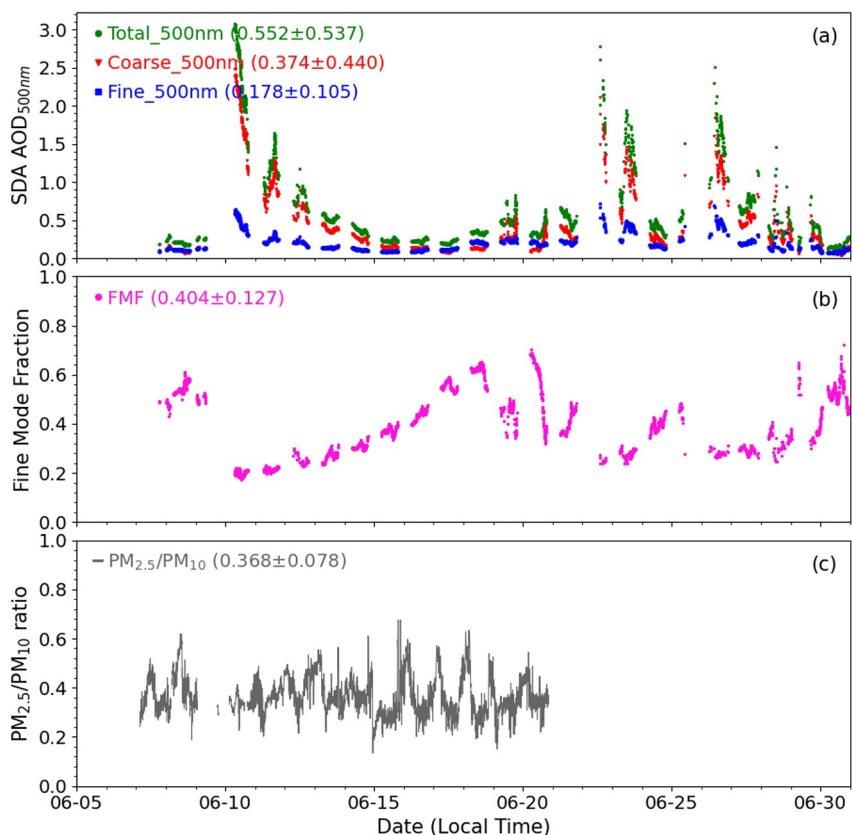
instantaneous  $AE_{440-870\text{ nm}}$  versus  $AOD_{500\text{ nm}}$  and the negative of the second derivative of  $\ln(AOD)$  with  $\ln(\alpha)$  versus  $AOD_{500\text{ nm}}$  acquired using a photometer at Ayvay during June of 2023. The  $AE_{440-870\text{ nm}}$  values exhibit a closely correlative relationship with  $AOD_{500\text{ nm}}$  during the period. That is, low  $AE_{440-870\text{ nm}}$  values ( $<0.60$ ) generally correspond to high  $AOD_{500\text{ nm}}$  ( $>0.30$ ), suggesting the dominance of coarse-mode dust aerosols, and large  $AE_{440-870\text{ nm}}$  values ( $>0.60 \sim 1.0$ ) commonly correspond to low  $AOD_{500\text{ nm}}$  ( $<0.3$ ), implying pristine background levels of aerosol concentration. The clear-sky and dust episode cases at Ayvay account for about 25% and 75% of the total days in June, respectively. The  $\alpha'$  is defined as the negative of the second derivative of  $\ln(AOD)$  with  $\ln\lambda$  that is a logical complement to the Ångström exponent and is used to quantify the relative influence of the accumulation model versus coarse-mode particles on aerosol optical properties. The  $\alpha'$  can be expressed as (Eck et al., 1999)

$$\alpha'(\lambda_i) = \frac{d\alpha}{d\lambda} = -\left(\frac{2}{\ln \lambda_{i+1} - \ln \lambda_{i-1}}\right) \cdot \left(\frac{\ln \tau_{a_{i+1}} - \ln \tau_{a_i}}{\ln \lambda_{i+1} - \ln \lambda_i} - \frac{\ln \tau_{a_i} - \ln \tau_{a_{i-1}}}{\ln \lambda_i - \ln \lambda_{i-1}}\right) \quad (3)$$

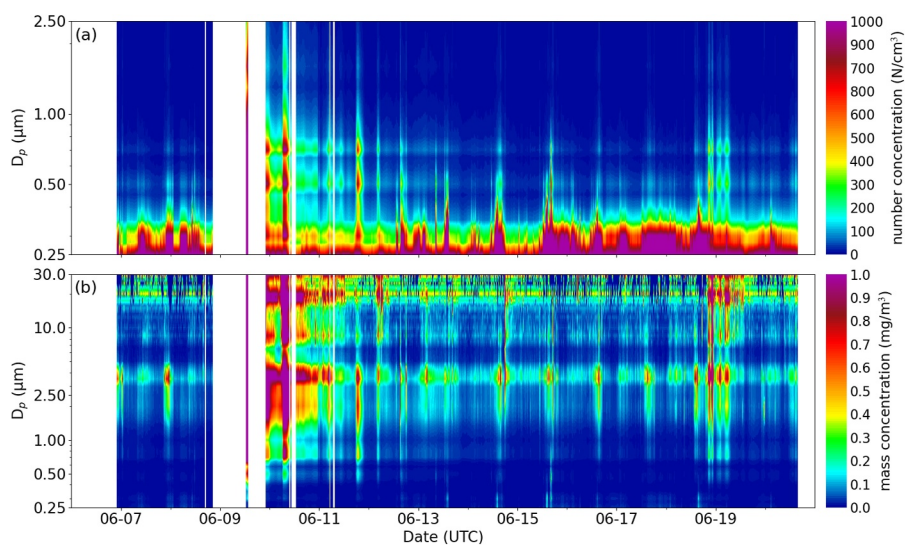
where  $\lambda_{i-1}$ ,  $\lambda_i$ , and  $\lambda_{i+1}$  are the wavelengths of 440, 675, and 870 nm, respectively.

From Figure 9b, the curvatures of  $\ln(AOD)$  and  $\ln\lambda(\alpha')$  are very low when coarse-mode dust particles strikingly dominate, which is consistent with the results in Figure 9a. And large curvature values (i.e., the absolute value of  $\alpha'$ ) indicate that small accumulation mode particles are dominant. Consequently, based on these pronounced relationships, we could quantitatively differentiate the dust aerosols from background aerosols species in Central Asia.

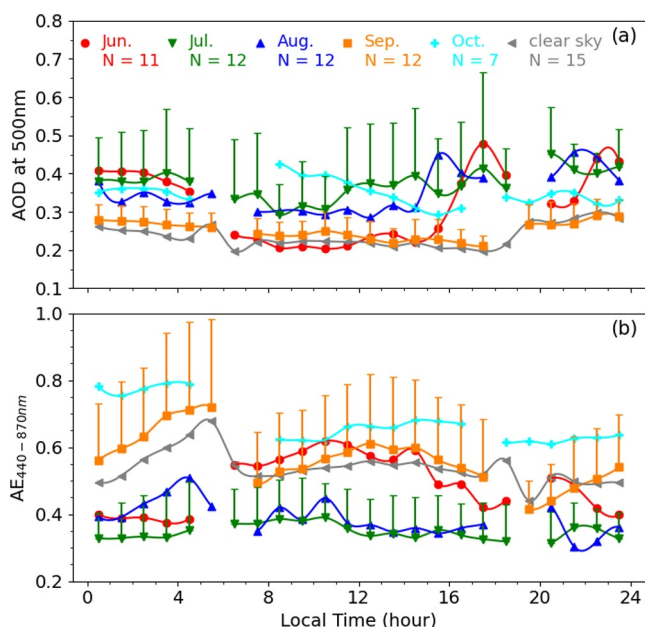
Figure 10 characterizes the time series of total, SDA coarse-mode and fine-mode  $AOD_{500\text{ nm}}$ , and fine-mode fraction (FMF) derived using a Cimel#1627 photometer, and the ratio of  $PM_{2.5}$  to  $PM_{10}$  at Ayvay during June of 2023. It is clear that the fine-mode  $AOD_{500\text{ nm}}$  values are commonly small and nearly invariant, while coarse-mode  $AOD_{500\text{ nm}}$  exhibit dramatic diurnal variations. There are only a few cases of fine-mode  $AOD_{500\text{ nm}}$  values to be comparable with the coarse-mode  $AOD_{500\text{ nm}}$  ( $0.08 \sim 0.23$ ) under clean and cloudless situations (e.g., from 15 to 18 June). In contrast, the coarse-mode  $AOD_{500\text{ nm}}$  values present drastic fluctuations and remain very high levels ( $0.80 \sim 2.48$ ) under heavy dust events (e.g., 9 to 12 June). The time series of total and coarse-mode  $AOD_{500\text{ nm}}$  values show a consistent change with the surface  $PM_{10}$  and  $PM_{2.5}$  mass concentrations. Fine-mode fraction is defined as the fine-mode  $AOD_{500\text{ nm}}$  values divided by total  $AOD_{500\text{ nm}}$ , which can well characterize the quantitative contribution of fine-mode or coarse-mode aerosols to total AOD. Fine-mode fraction values in Ayvay vary from 0.17 to 0.72 and remain low and constant ( $0.17 \sim 0.31$ ) under heavy dust events (i.e., 9–12, 23, and 25–28 June). The ratios of  $PM_{2.5}/PM_{10}$  display similar diurnal variation features with that of FMF. The overall average values of total, coarse- and fine-mode  $AOD_{500\text{ nm}}$ , FMF, and ratio of  $PM_{2.5}/PM_{10}$  are  $0.552 \pm 0.537$ ,  $0.374 \pm 0.440$ ,  $0.178 \pm 0.105$ ,  $0.404 \pm 0.127$ , and  $0.368 \pm 0.078$ , respectively. Our results once again firmly corroborate that large dust particles are the major contributors to total aerosol loading in Ayvay during June 2023.



**Figure 10.** Time series of (a) total (green circle), spectral deconvolution algorithm (SDA) and coarse-mode (red triangle) and fine-mode (blue square) AOD at 500 nm, (b) fine-mode fraction (FMF) acquired using a Cimel#1627 photometer, and (c) the ratio of PM<sub>2.5</sub> to PM<sub>10</sub> at Ayvay in June of 2023. The overall average value and one standard deviation are in parentheses.



**Figure 11.** Time evolutions of five-minute averaged aerosol (a) number concentration ( $dN/d\log D_p$  in  $N/cm^3$ ) and (b) mass concentration ( $dM/d\log D_p$  in  $mg/m^3$ ) with aerosol size distribution measured using a GRIMM particle sizer spectrometer at Ayvay from 8 to 20 June to 2023.



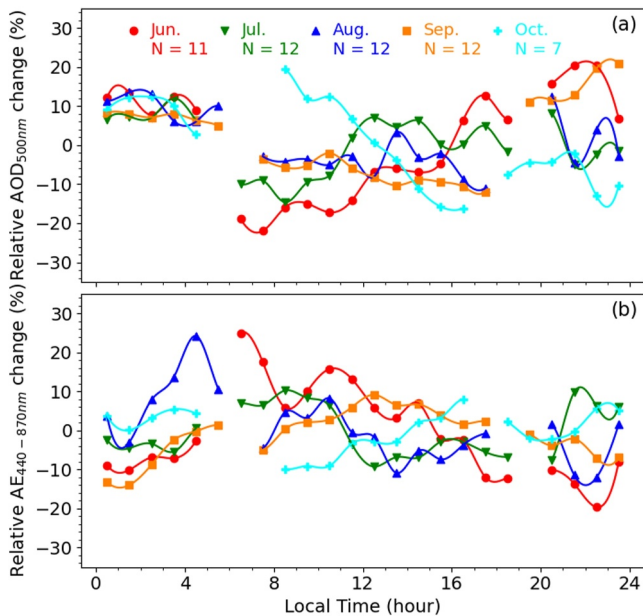
**Figure 12.** Diurnal cycle of hourly mean (a)  $AOD_{500\text{ nm}}$  and (b)  $AE_{440-870\text{ nm}}$  for various months and 15 clear-sky days obtained using a Cimel#1627 photometer at Ayvaj from June to October 2023.  $N$  is the total number of days for valid data points in each month. The error bars of July and September indicate plus or minus one standard deviation, and those for the other months are not shown.

Figure 11 displays the time evolutions of five-minute averaged aerosol number concentration ( $dN/d\log D_p$ ) and mass concentration ( $dM/d\log D_p$ ) with aerosol size distribution measured using a GRIMM sizer spectrometer in Ayvaj from 8 to 20 June of 2023. The  $dN/d\log D_p$  exhibits a noticeable diurnal change during the period, and varies from 200 to 2500  $N/cm^3$  in 0.25–0.40  $\mu m$  size range and from 50 to 800  $N/cm^3$  in 0.40–2.5  $\mu m$ . A discernible feature is shown in Figure 11a that  $dN/d\log D_p$  presents a relatively uniform high concentration from 0.25 to 10  $\mu m$  under heavy dust events (i.e., 9–10 June), with  $dN/d\log D_p$  from 1,000 to 3600  $N/cm^3$  in 0.25–1.0  $\mu m$  and from 100 to 900  $N/cm^3$  in 1.0–10  $\mu m$ . Although the  $dN/d\log D_p$  of coarse-mode aerosol particles are about two to three orders of magnitude smaller than those of fine particles ( $<1.0\ \mu m$ ), the mass density and volume of the former are the same magnitude greater than those of the latter, resulting in a higher aerosol mass concentration of large particles than the fine particles. Consequently, the  $dM/d\log D_p$  distributions exhibit a distinct bimodal pattern and vary from 20 to 1,000  $\mu g/m^3$  during the period, and corresponding particle diameter ( $D_p$ ) is mainly concentrated in the ranges of 1.0–5.0 and 15–25  $\mu m$ , with the peak diameters of 3.0–5.0 and 20  $\mu m$ , respectively. It is evident that  $dM/d\log D_p$  also shows extremely high concentrations in the entire spectrum range under strong dust episodes on 9th June and change from 500 to 3,000  $\mu g/m^3$  in the size ranges of 1.0–5.0 and 10–30  $\mu m$ , and from 100 to 500  $\mu g/m^3$  in the other wave bands. Sviridenkov et al. (1993) have documented that dust aerosols in Shaartuz showed a log-normal distribution and the corresponding volume number and mass concentrations had the median diameters of 0.5  $\mu m$  and 3.5–6.0  $\mu m$ , respectively, during a strong dust storm on 20th September 1989, which is close to our in situ measurement results. This provides a direct observational evidence to demonstrate that surface aerosol particulates are overwhelmingly dominated by coarse-mode dust particles at Ayvaj in June 2023.

#### 4.4. Diurnal Variability of Hourly Mean AODs

In this section, the hourly averages of aerosol optical parameters are calculated via the arithmetic mean of all individual observations within 1 hour (00:00–01:00, 01:00–02:00 local time, etc.) for each day. The daily averages are computed from all available hourly means for each day when more than six hourly means are available. A percentage departure is derived from all individual observations minus the corresponding daily mean value, and the hourly averaged percentage deviation is averaged hourly (05:00–06:00, 07:00–08:00 local time, etc.) for a given month (Smirnov et al., 2002; Zhang et al., 2012). Thus, we can acquire the systematic diurnal cycles of hourly mean and percentage deviations of aerosol optical parameters for diverse months. Here, we show diurnal variability of  $AOD_{500\text{ nm}}$  and  $AE_{440-870\text{ nm}}$ , unless otherwise noted.

Figure 12 depicts diurnal cycle of hourly mean  $AOD_{500\text{ nm}}$  and  $AE_{440-870\text{ nm}}$  for various months and 15 clear-sky days obtained using a Cimel#1627 photometer in Ayvaj from June to October 2023.  $N$  is the total number of days for valid data points in each month. The diurnal variations of  $AOD_{500\text{ nm}}$  exhibit a prominent characteristic with relatively stable and low values in daytime and fluctuating high values in nighttime. The diurnal dependence in September is fairly small and  $AOD_{500\text{ nm}}$  vary within 0.21 ~ 0.25 range in daytime (07:00–17:00) and 0.26 ~ 0.29 in nighttime (19:00–05:00), respectively, which is perfectly consistent with the diurnal cycle of 15 clear-sky days. This result unravels that the aerosol optical properties in September can well represent the pristine background levels at Ayvaj. Note that the daytime (06:00–15:00)  $AOD_{500\text{ nm}}$  in June also remains at a stable background level (0.20 ~ 0.25), while they show dramatic fluctuations and high values (0.32 ~ 0.48) during the afternoon–nighttime period (16:00–04:00), with the maximum value of 0.48 appearing at 18:00. By contrast, the diurnal changes of  $AOD_{500\text{ nm}}$  in July and August present larger values and comparably sharp fluctuations, within 0.29 ~ 0.45 range, which is mainly attributable to the significant contributions of frequent dust events at Ayvaj. The results of this study suggest that if the daily mean values of AOD are calculated using only daytime values at Ayvaj, and the nocturnal AODs are ignored, which will lead to a big uncertainty in evaluating aerosol radiative forcing in regional climate models. The diurnal variations of  $AE_{440-870\text{ nm}}$  exhibit an opposite pattern to that of



**Figure 13.** Percentage deviations of hourly averaged (a)  $AOD_{500\text{ nm}}$  and (b)  $AE_{440-870\text{ nm}}$  relative to the daily mean in each month obtained using a Cimel#1627 photometer at Ayvaj from June to October 2023. N is the total number of days for valid data points in each month.

AODs at Ayvaj. For instance, the percentage departure of  $AOD_{500\text{ nm}}$  varies from  $-22\% \sim -5\%$  during daytime to  $6\% \sim 22\%$  during nighttime in June and corresponding  $AE_{440-870\text{ nm}}$  changes from  $-2\% \sim 25\%$  to  $-20\% \sim -2\%$ , respectively. And high values of the absolute percentage departure are well consistent with high AODs (i.e., strong dust episodes). The percentage departures of both  $AOD_{500\text{ nm}}$  and  $AE_{440-870\text{ nm}}$  in one hour could reach up to 10% of the daily mean. As shown in Figure 13a, the  $AOD_{500\text{ nm}}$  departure from daily mean at 15:00 p.m. in June is about  $-4\%$  and increases to  $6\%$  at 16:00 p.m. and  $12\%$  at 17:00 p.m., respectively. Such significant differences between daytime and nighttime have not been reported previously, majorly due to the lack of nocturnal observations of lunar irradiances in Central Asia. Our results are well in accordance with the daytime diurnal variability of dust AOD and an Ångström exponent over a dust source region in Northwest China (Wang et al., 2004). Nevertheless, Smirnov et al. (2002) revealed that diurnal variability range of dust AOD is normally smaller than  $\pm 5\%$  over AERONET sites where dust is a main contributor to AOD, which is much lower than the results of this study. The major reasons for the discrepancy are owing to the different geographical locations and meteorological conditions at diverse desert source sites. Another pronounced feature is that both  $AOD_{500\text{ nm}}$  and  $AE_{440-870\text{ nm}}$  departures change drastically and often abruptly from daily positive values to negative values in the last 2 ~ 3 hr after sunset or moonset. This may be attributed to the fact that high AOD values frequently appear at the afternoon–nighttime period. In addition, photometric measurements have a greater chance of cloud contamination at low solar elevation angles or MPAs during the period (Giles et al., 2019; Smirnov et al., 2000). The other simultaneous lidar and meteorological data sets are called for further interpreting these rapid changes. Such significant diurnal variations of dust aerosol optical properties should be considered in the calculations of its diurnal radiative forcing and climatic effects.

#### 4.5. Monthly Variations of Daytime and Nocturnal AODs

In order to ensure the representativeness of statistical metrics, we only compute the daily mean values of daytime and nocturnal aerosol optical properties, respectively, when both daytime and nighttime AODs have an effective number of data points. And the corresponding monthly averages are calculated from all daily mean values for each month and characterize the major statistical results of both data sets.

Figure 14 delineates the box plots of monthly mean daytime and nighttime  $AOD_{440\text{ nm}}$  and  $AOD_{870\text{ nm}}$  at Ayvaj. Circles and horizontal bold lines in each box indicate the mean and median values, respectively. The lower and upper boundaries of each box denote the 25th and 75th percentile, respectively. The whiskers represent the 5th and

$AOD_{500\text{ nm}}$ . More specifically, the diurnal behaviors of  $AE_{440-870\text{ nm}}$  keep invariant and low values during active dust seasons (i.e., July and August) and vary from 0.32 to 0.39 throughout the hourly mean periods in July, implying that the coarse large dust particles are predominant. In contrast, the hourly average  $AE_{440-870\text{ nm}}$  in September shows a moderate value of  $0.49 \sim 0.62$  during daytime (07:00–17:00), and ranges from 0.44 to 0.53 before the midnight (19:00–23:00) and remains within  $0.56 \sim 0.72$ , which indicates that different aerosol particle sizes dominate in different time periods. The mean  $AE_{440-870\text{ nm}}$  values in June and October also present a significant diurnal dependence, but are somewhat different from those in July and September, as shown in Figure 12b. Meanwhile, the corresponding standard deviations increase evidently with the increase of AOD or  $AE_{440-870\text{ nm}}$  values.

Compared with the hourly average, a percentage departure enables systematic diurnal trends more evident. Figure 13 shows percentage deviations of hourly averaged  $AOD_{500\text{ nm}}$  and  $AE_{440-870\text{ nm}}$  relative to the daily mean in each month obtained using a photometer in Ayvaj during the whole period. The percentage departures of  $AOD_{500\text{ nm}}$  ( $AE_{440-870\text{ nm}}$ ) present systematically lower (larger) during the daytime (06:00–18:00 local time) and larger (lower) in the nighttime (19:00–05:00 local time). In all months, the relative diurnal changes of  $AOD_{500\text{ nm}}$  are commonly greater than  $-22\%$  in daytime and smaller than  $+22\%$  in nighttime (equivalent to a change of AOD about 0.10), and corresponding  $AE_{440-870\text{ nm}}$  are about  $-20\% \sim +25\%$ . The prevalent dust storms exert an important role in modulating diurnal variability of spectral

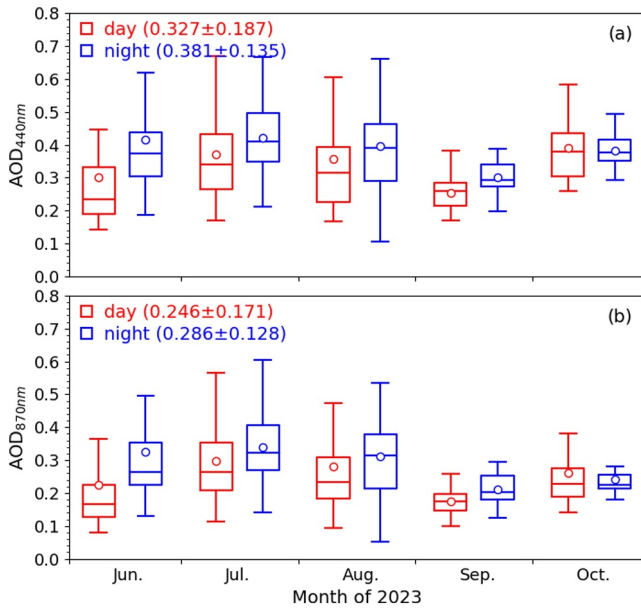


**Figure 14.** Monthly mean daytime (red boxes) and nighttime (blue boxes) (a) AOD<sub>440 nm</sub> and (b) AOD<sub>870 nm</sub> at Ayvaj. Circles and horizontal bold lines indicate the mean and median values, respectively. The lower and upper boundary of each box denote the 25th and 75th percentile, respectively. The whiskers represent the 5th and 95th percentile, respectively. The overall average value and one standard deviation are in parentheses.

0.472 ± 0.192 and 0.467 ± 0.200, respectively, which are evidently lower than the daytime average of 0.52 ~ 0.54 in Dushanbe for June–August 2015–2016 (Hofer et al., 2017). This further unveils that dust aerosols is the dominant atmospheric aerosol type in the Ayvaj region during June–August 2023, and the contribution of background fine-mode particles in other nondusty seasons becomes more pronounced (i.e., with larger AE<sub>440–870 nm</sub>) than that in dusty seasons.

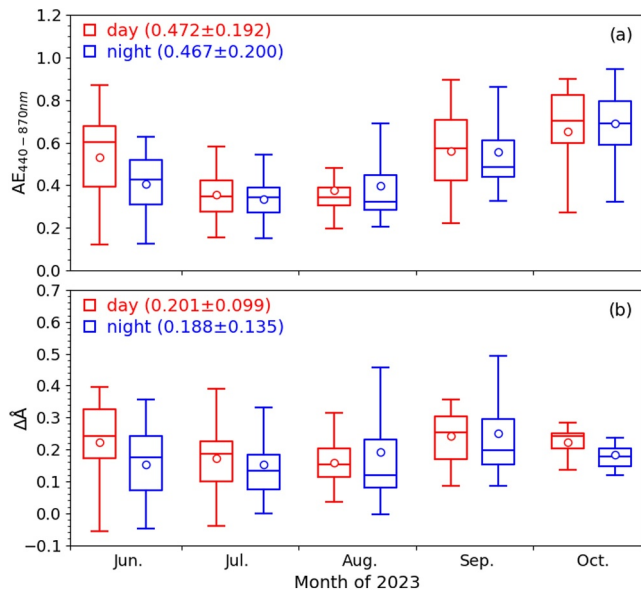


**Figure 15.** The same as Figure 14, except for monthly mean daytime and nighttime AE<sub>440–870 nm</sub> and ΔÅ derived using a Cimel#1627 photometer at Ayvaj. ΔÅ value is calculated as the difference between AE<sub>440–675 nm</sub> and AE<sub>675–870 nm</sub>.

95th percentile. The overall average value and one standard deviation are in parentheses. In general, both daytime and nighttime AOD<sub>440 nm</sub> and AOD<sub>870 nm</sub> values show a similar monthly variation characteristic. Namely, the mean AODs in prevailing dust seasons from June to August (AOD<sub>440 nm</sub> of 0.25 ~ 0.51) are clearly higher than the ones (AOD<sub>440 nm</sub> of 0.16 ~ 0.45) in September and October. The monthly mean AODs are mostly greater than the corresponding median values both at 440 and 870 nm, and all nocturnal AOD values are almost bigger than corresponding daytime AODs. Both daytime and nighttime AOD<sub>440 nm</sub> values are on average 33% larger than those of AOD<sub>870 nm</sub>. The overall average daytime and nighttime AOD<sub>440 nm</sub> values are 0.327 ± 0.187 and 0.381 ± 0.135, respectively, and corresponding AOD<sub>870 nm</sub> values are 0.246 ± 0.171 and 0.286 ± 0.128, respectively. A high variable range of percentiles from June to August reflects the dramatic day-to-day variability of daytime and nighttime AODs during summer season at Ayvaj, attributable to the remarkable disturbance caused by intrusions of dust events.

Figure 15 is the same as Figure 14, except for monthly mean daytime and nighttime AE<sub>440–870 nm</sub> and ΔÅ derived using a Cimel#1627 photometer at Ayvaj. Obviously, the average AE<sub>440–870 nm</sub> values in two time periods exhibit an opposite monthly variation pattern with AODs. That is, the monthly average AE<sub>440–870 nm</sub> values from July to August remain low (0.28 ~ 0.45) and the amplitudes of variation are smaller, whereas the mean AE<sub>440–870 nm</sub> values in September and October vary from 0.42 to 0.85, and corresponding amplitudes of variation range from 0.20 to 1.0. Additionally, all nighttime AE<sub>440–870 nm</sub> values are less than corresponding daytime AE<sub>440–870 nm</sub>. The total mean daytime and nocturnal AE<sub>440–870 nm</sub> values are 0.472 ± 0.192 and 0.467 ± 0.200, respectively, which are evidently lower than the daytime average of 0.52 ~ 0.54 in Dushanbe for June–August 2015–2016 (Hofer et al., 2017). This further unveils that dust aerosols is the dominant atmospheric aerosol type in the Ayvaj region during June–August 2023, and the contribution of background fine-mode particles in other nondusty seasons becomes more pronounced (i.e., with larger AE<sub>440–870 nm</sub>) than that in dusty seasons. ΔÅ is denoted as the spectral variation of the Ångström exponent, and it can supply useful information on the qualitative contribution of fine- and coarse-mode particles (Schuster et al., 2006). The ΔÅ value is calculated as the difference between AE<sub>440–675 nm</sub> and AE<sub>675–870 nm</sub>. The negative ΔÅ values stand for the dominance of a single fine-mode particle, while positive ΔÅ values indicate the combined effect of two independent particle modes, and more specifically, that ΔÅ increases with the contribution of coarse-mode particles (Perrone et al., 2022; Schuster et al., 2006). From Figure 15b, it is apparent that daytime and nighttime ΔÅ show similar monthly change characteristics with AE<sub>440–675 nm</sub>, but there are some numerical differences. All ΔÅ values are positive and vary from 0.07 to 0.33, and the daytime ΔÅ values are slightly larger than those in nighttime, with the overall averages of 0.201 ± 0.099 and 0.188 ± 0.135, respectively. These results uncover that the contribution of coarse-mode dust particle on total aerosol loading is significantly high at Ayvaj during June–October 2023, mainly due to the influences of frequent incursions of dust events during the period.

## 5. Concluding Remarks

For the first time, this paper mainly investigated the diurnal and nocturnal dust aerosol characteristics during June–October 2023 at Ayvaj of southwest Tajikistan determined from CE318-T sun-sky-lunar photometric measurements. Both the daytime and nighttime AOD values were well consistent with synchronous observations of a collocated lidar. The major conclusions can be summarized as follows.

The ROLO-RCF method was capable of reliably calculating nocturnal AODs and the Ångström exponent from CE318-T measurements at Ayvaj, regardless of different levels of aerosol loadings. The AOD day/night transition coherence test has persuasively corroborated the reliability of multispectral nighttime AOD values acquired using a CE318-T photometer at both night-to-day and day-to-night time intervals. The results indicated that the absolute differences of  $\Delta\text{AOD}_{\text{MR}}$  and  $\Delta\text{AOD}_{\text{MS}}$  at 500 nm varied within the ranges of (0.007 ~ 0.051) and (0.001 ~ 0.061), respectively, which were slightly greater but fell within the accuracy level of lunar AODs (Barreto et al., 2019; Bi et al., 2024) and solar AODs (Giles et al., 2019). Both  $\text{AOD}_{\text{moonrise}}$  and  $\text{AOD}_{\text{sunset}}$  ( $\text{AOD}_{\text{moonset}}$  and  $\text{AOD}_{\text{sunrise}}$ ) values as well as corresponding  $\text{AE}_{440-870 \text{ nm}}$  at Ayvaj showed an excellent consistency and corresponding RMSEs, MBs, and linear fitting regressions all were in favor of the reliability nocturnal AOD values.

In general, both spectral AOD values and  $\text{AE}_{440-870 \text{ nm}}$  exhibited a prominent diurnal variation and nocturnal AOD values presented a good continuity with daytime AODs in a wide range of Moon's illuminations under stable changes of aerosol loading. This is crucial to form a complete picture of aerosol climatology. The prevalent dust events occurred frequently in Ayvaj from June to August 2023, which produced a significant influence on columnar aerosol optical properties and near-surface particle size distributions on a regional scale. The maximal  $\text{AOD}_{500 \text{ nm}}$ ,  $\text{PM}_{2.5}$ , and  $\text{PM}_{10}$  mass concentrations under a strong dust storm on 9–10 June 2023 were 3.07, 2,800, and 9,400  $\mu\text{g}/\text{m}^3$ , respectively, and corresponding  $\text{AE}_{440-870 \text{ nm}}$ , FMF, and ratio of  $\text{PM}_{2.5}/\text{PM}_{10}$  were 0.01, 0.17, and 0.24, respectively, suggesting that large dust particles were the dominant aerosol type in Ayvaj during the period.

The diurnal cycles of hourly mean  $\text{AOD}_{500 \text{ nm}}$  remained steady low values (0.20 ~ 0.25) in daytime and showed larger values (0.32 ~ 0.48) and sharp fluctuations in nighttime, while the  $\text{AE}_{440-870 \text{ nm}}$  displayed an opposite feature. Consequently, the percentage departures of  $\text{AOD}_{500 \text{ nm}}$  revealed systematically negative values (−22% ~ −5%) during daytime and positive values (+6% ~ +25%) in nighttime and corresponding  $\text{AE}_{440-870 \text{ nm}}$  ranged within  $\pm 25\%$ . Meanwhile, the diurnal departures of both  $\text{AOD}_{500 \text{ nm}}$  and  $\text{AE}_{440-870 \text{ nm}}$  changed drastically and often abruptly from daily positive value (+12%) to negative value (−5%) in the last 2 ~ 3 hr after sunset or moonset, probably attributable to the high AOD values, which usually appeared at the afternoon–nighttime period triggered by frequent intrusion of dust events. The simultaneous lidar and meteorological data sets were called for further elucidating such rapid changes. Both the mean daytime and nighttime spectral AODs showed a similar monthly variation characteristic and average AOD values in prevailing dust seasons from June to August ( $\text{AOD}_{440 \text{ nm}}$  of 0.25 ~ 0.51) were generally greater than the ones ( $\text{AOD}_{440 \text{ nm}}$  of 0.16 ~ 0.45) in September and October. The monthly mean AODs were mostly larger than corresponding median values both at 440 and 870 nm, and all nocturnal AOD values were almost bigger than corresponding daytime AODs. In contrast, the monthly average daytime and nighttime  $\text{AE}_{440-870 \text{ nm}}$  and  $\Delta\text{Å}$  values remained relatively stable and low (0.28 ~ 0.45 and 0.07 ~ 0.33) from July to August, but were maintained as fluctuating and high (0.42 ~ 0.85 and 0.15 ~ 0.30) in September and October. The overall average daytime and nighttime  $\text{AOD}_{440 \text{ nm}}$  values were  $0.327 \pm 0.187$  and  $0.381 \pm 0.135$ , respectively, and corresponding  $\text{AE}_{440-870 \text{ nm}}$  were  $0.472 \pm 0.192$  and  $0.467 \pm 0.200$ , implying that coarse-mode dust particles were the main contributors to total aerosol loading in Ayvaj during the whole period.

In summary, this study confirmed that a CE318-T photometer had a unique capability to measure nocturnal aerosol optical parameters under a wide range of Moon's phase cycles in a typical semidesert region of Central Asia. Both the daytime and nighttime AODs obtained using a CE318-T photometer not only can afford favorable physical constraints to improve the precise solution of current Mie scattering lidar equation, but also provide a high-quality ground truth to validate geostationary satellite aerosol products in bright surface desert areas, and to quantitatively evaluate the potential impacts of dust aerosols on air quality, transboundary transport, and environment in Central Asia. The remarkable diurnal variability of dust AODs and  $\text{AE}_{440-870 \text{ nm}}$  disparity at Ayvaj found in this study should be included in regional climate models to simulate its diurnal radiative forcing in the future work.

### Data Availability Statement

All data sets used in this study can be freely accessible to the public at Wang (2024). The standard extraterrestrial solar irradiance spectrum used in this study can be freely accessible to the public at Wehrli (1985).

**Acknowledgments**

This work is jointly supported by the National Natural Science Foundation of China (42075126, W2411029), Gansu Provincial Science and Technology Innovative Talent Program: High-level Talent and Innovative Team Special Project (Chief Scientist System, No. 22JR9KA001), and Fundamental Research Funds for the Central Universities (Izujbky-2024-jdzx04), and the China 111 Project (B13045). The authors would like to express special thanks to all staff of Hydrometeorological Service of Tajikistan for supporting the field experiment. We are grateful to the United States Geological Survey (USGS) as a NASA-funded project for supplying the ROLo model used in this study. We also appreciate the editors and all peer reviewers for their insightful and valuable comments.

**References**

Abdullaev, S. F., Maslov, V. A., Nazarov, B. I., & Salikhov, T. K. (2014). Variations in parameters of aerosol optical thickness in Dushanbe. *Atmos. Ocean Phys.*, 50(4), 431–434. <https://doi.org/10.1134/s0001433814030025>

Abdullaev, S. F., & Sokolik, I. N. (2019). Main characteristics of dust storms and their radiative impacts: With a focus on Tajikistan. *J. Atmos. Sci. Res.*, 2(2), 1–21. <https://doi.org/10.30564/jasr.v2i2.352>

Andronova, A. V., Gomes, L., Smirnov, V. V., Ivanov, A. V., & Shhukurova, L. M. (1993). Physico-chemical characteristics of dust aerosols deposited during the Soviet-America (Tadzhikistan, 1989). *Atmospheric Environment*, 27A(16), 2487–2493.

Arola, A., Eck, T. F., Huttunen, J., Lehtinen, K. E. J., Lindfors, A. V., Myhre, G., et al. (2013). Influence of observed diurnal cycles of aerosol optical depth on aerosol direct radiative effect. *Atmospheric Chemistry and Physics*, 13(15), 7895–7901. <https://doi.org/10.5194/acp-13-7895-2013>

Baibakov, K., O’Neil, N. T., Ivanescu, L., Duck, T. J., Perro, C., Herber, A., et al. (2015). Synchronous polar winter starphotometry and lidar measurements at a High Arctic station. *Atmospheric Measurement Techniques*, 8(9), 3789–3809. <https://doi.org/10.5194/amt-8-3789-2015>

Barreto, Á., Cuevas, E., Damiri, B., Guirado, C., Berkoff, T., Berjón, A. J., et al. (2013). A new method for nocturnal aerosol measurements with a lunar photometer prototype. *Atmospheric Measurement Techniques*, 6(3), 585–598. <https://doi.org/10.5194/amt-6-585-2013>

Barreto, Á., Cuevas, E., Granados-Munñoz, M.-J., Alados-Arboledas, L., Romero, P. M., Gröbner, J., et al. (2016). The new Sun-sky-lunar Cimel CE318-T multiband photometer—a comprehensive performance evaluation. *Atmospheric Measurement Techniques*, 9(2), 631–654. <https://doi.org/10.5194/amt-9-631-2016>

Barreto, Á., Román, R., Cuevas, E., Berjón, A. J., Almansa, A. F., Toledano, C., et al. (2017). Assessment of nocturnal aerosol optical depth from lunar photometry at the Izaña high mountain observatory. *Atmospheric Measurement Techniques*, 10(8), 3007–3019. <https://doi.org/10.5194/amt-10-3007-2017>

Barreto, Á., Román, R., Cuevas, E., Pérez-Ramírez, D., Berjón, A. J., Kouremeti, N., et al. (2019). Evaluation of night-time aerosols measurements and lunar irradiance models in the frame of the first multi-instrument nocturnal intercomparison campaign. *Atmospheric Environment*, 202, 190–211. <https://doi.org/10.1016/j.atmosenv.2019.01.006>

Berkoff, T. A., Sorokin, M., Stone, T., Eck, T. F., Hoff, R., Welton, E., & Holben, B. (2011). Nocturnal aerosol optical depth measurements with a small-aperture automated photometer using the moon as a light source. *Journal of Atmospheric and Oceanic Technology*, 28(10), 1297–1306. <https://doi.org/10.1175/JTECH-D-10-05036.1>

Bi, J., Huang, J., Holben, B., & Zhang, G. (2016). Comparison of key absorption and optical properties between pure and transported anthropogenic dust over East and Central Asia. *Atmospheric Chemistry and Physics*, 16(24), 15501–15516. <https://doi.org/10.5194/acp-16-15501-2016>

Bi, J., Huang, J., Shi, J., Hu, Z., Zhou, T., Zhang, G., et al. (2017). Measurement of scattering and absorption properties of dust aerosol in a Gobi farmland region of northwestern China—A potential anthropogenic influence. *Atmospheric Chemistry and Physics*, 17(12), 7775–7792. <https://doi.org/10.5194/acp-17-7775-2017>

Bi, J., Li, B., Ma, J., Wang, X., Meng, Z., Shi, J., & Li, Z. (2024). Evaluation of nocturnal aerosol optical depth determining from a lunar photometry in Lanzhou of northwest China. *Journal of Geophysical Research: Atmospheres*, 129(12), e2023JD040387. <https://doi.org/10.1029/2023JD040387>

Bi, J., Shi, J., Xie, Y., Liu, Y., Takamura, T., & Khatri, P. (2014). Dust aerosol characteristics and shortwave radiative impact at a Gobi Desert of Northwest China during the spring of 2012. *Journal of the Meteorological Society of Japan*, 92A(0), 33–56. <https://doi.org/10.2151/jmsj.2014-A03>

Che, H., Xia, X., Zhao, H., Li, L., Gui, K., Zheng, Y., et al. (2024). Aerosol optical and radiative properties and their environmental effects in China: A review. *Earth-Science Reviews*, 248, 104634. <https://doi.org/10.1016/j.earscirev.2023.104634>

Chen, L., Liu, C., Wang, J., Chen, G., Zhao, Y., Jin, Y., & Jin, H. (2025). How is the spatiotemporal representativeness of ground- and satellite-based aerosol optical depth (AOD) measurements over Asia? *Atmospheric Research*, 315, 107857. <https://doi.org/10.1016/j.atmosres.2024.107857>

Christopher, S. A., Wang, J., Ji, Q., & Tsay, S.-C. (2003). Estimation of diurnal shortwave dust aerosol radiative forcing during PRIDE. *Journal of Geophysical Research*, 108(D19), 8596. <https://doi.org/10.1029/2002JD002787>

Dong, Q., Huang, Z., Li, W., Li, Z., Song, X., Liu, W., et al. (2022). Polarization lidar measurements of dust optical properties at the junction of the Taklimakan desert–Tibetan Plateau. *Remote Sensing*, 14(3), 558. <https://doi.org/10.3390/rs14030558>

Dubovik, O., Holben, B. N., Eck, T. F., Smirnov, A., Kaufman, Y. J., King, M. D., et al. (2002). Variability of absorption and optical properties of key aerosol types observed in worldwide locations. *Journal of the Atmospheric Sciences*, 59(3), 590–608. [https://doi.org/10.1175/1520-0469\(2002\)059<0590:voaaoop>2.0.co;2](https://doi.org/10.1175/1520-0469(2002)059<0590:voaaoop>2.0.co;2)

Eck, T. F., Holben, B. N., Seid, J. S., Dubovik, O., Smirnov, A., O’Neill, N. T., et al. (1999). Wavelength dependence of the optical depth of biomass burning, urban and desert dust aerosols. *Journal of Geophysical Research*, 104(D24), 31333–31349. <https://doi.org/10.1029/1999JD900923>

Giles, D. M., Sinyuk, A., Sorokin, M. G., Schafer, J. S., Smirnov, A., Slutsker, I., et al. (2019). Advancements in the Aerosol Robotic Network (AERONET) Version 3 database-automated near-real-time quality control algorithm with improved cloud screening for Sun photometer aerosol optical depth (AOD) measurements. *Atmospheric Measurement Techniques*, 12(1), 169–209. <https://doi.org/10.5194/amt-12-169-2019>

Gillette, D. A., Bodhaine, B. A., & Mackinnon, D. (1993). Transport and deposition of desert dust in the Kafirnigan River Valley (Tadzhikistan) from Shaartuz to Esanbay: Measurements and a simple model. *Atmospheric Environment*, 27A(16), 2545–2552. [https://doi.org/10.1016/0960-1686\(93\)90028-w](https://doi.org/10.1016/0960-1686(93)90028-w)

Golitsyn, G., & Gillette, D. A. (1993). Introduction: A joint Soviet-American experiment for the study of Asian desert dust and its impact on local meteorological conditions and climate. *Atmospheric Environment*, 27A(16), 2467–2470. [https://doi.org/10.1016/0960-1686\(93\)90017-s](https://doi.org/10.1016/0960-1686(93)90017-s)

Grimm, H., & Eatough, D. J. (2009). Aerosol measurement: The use of optical light scattering for the determination of particulate size distribution, and particulate mass, including the semi-volatile fraction. *Journal of the Air & Waste Management Association*, 59(1), 101–107. <https://doi.org/10.3155/1047-3289.59.1.101>

Hofer, J., Althausen, D., Abdullaev, S. F., Makhmudov, A. N., Nazarov, B. I., Schettler, G., et al. (2017). Long-term profiling of mineral dust and pollution aerosol with multiwavelength polarization Raman lidar at the Central Asian site of Dushanbe, Tajikistan: Case studies. *Atmospheric Chemistry and Physics*, 17(23), 14559–14577. <https://doi.org/10.5194/acp-17-14559-2017>

Hofer, J., Ansmann, A., Althausen, D., Engelmann, R., Baars, H., Fomba, K. W., et al. (2020). Optical properties of Central Asian aerosol relevant for spaceborne lidar applications and aerosol typing at 355 and 532 nm. *Atmospheric Chemistry and Physics*, 20(15), 9265–9280. <https://doi.org/10.5194/acp-20-9265-2020>

- Huang, J., Fu, Q., Zhang, W., Wang, X., Zhang, R., Ye, H., & Warren, S. G. (2011). Dust and black carbon in seasonal snow across northern China. *Bulletin American Meteorology Sociol*, 92(2), 175–181. <https://doi.org/10.1175/2010BAMS3064.1>
- Huang, J., Lin, B., Minnis, P., Wang, T., Wang, X., Hu, Y., et al. (2006). Satellite-based Assessment of possible dust aerosols semi-direct effect on cloud water path over east Asia. *Geophysical Research Letters*, 33(19), L19802. <https://doi.org/10.1029/2006GL026561>
- Huang, J., Wang, T., Wang, W., Li, Z., & Yan, H. (2014). Climate effects of dust aerosols over East Asian arid and semiarid regions. *Journal of Geophysical Research*, 119(19), 11398–11416. <https://doi.org/10.1002/2014jd021796>
- Huang, X., Wang, Z., & Ding, A. (2018). Impact of aerosol-PBL interaction on Haze pollution: Multiyear observational evidences in north China. *Geophysical Research Letters*, 45(16), 8596–8603. <https://doi.org/10.1029/2018gl079239>
- Kang, S., Zhang, Q., Qian, Y., Ji, Z., Li, C., Cong, Z., et al. (2019). Linking atmospheric pollution to cryospheric change in the Third Pole region: Current progress and future prospects. *National Science Review*, 6(4), 796–809. <https://doi.org/10.1093/nsr/nwz031>
- Kayumov, A., & Novikov, V. (2014). Third national communication of the republic of Tajikistan under the. *United Nations Framework Convention on Climate Change*.
- Kieffer, H. H., & Stone, T. C. (2005). The spectral irradiance of the moon. *The Astronomical Journal*, 129(6), 2887–2901. <https://doi.org/10.1086/430185>
- Kuang, Y., Zhao, C., Tao, J., & Ma, N. (2015). Diurnal variations of aerosol optical properties in the North China Plain and their influences on the estimates of direct aerosol radiative effect. *Atmospheric Chemistry and Physics*, 15(10), 5761–5772. <https://doi.org/10.5194/acp-15-5761-2015>
- Kulmala, M., Kontkanen, J., Junninen, H., Lehtipalo, K., Manninen, H. E., Nieminen, T., et al. (2013). Direct observations of atmospheric aerosol nucleation. *Science*, 339(6122), 943–946. <https://doi.org/10.1126/science.1227385>
- Li, J., Carlson, B. E., Yung, Y. L., Lv, D., Hansen, J., Penner, J. E., et al. (2022). Scattering and absorbing aerosols in the climate system. *Nature Reviews Earth and Environment*, 3(6), 363–379. <https://doi.org/10.1038/s43017-022-00296-7>
- Li, Z., Guo, J., Ding, A., Liao, H., Liu, J., Sun, Y., et al. (2017). Aerosol and boundary-layer interactions and impact on air quality. *National Science Review*, 4(6), 810–833. <https://doi.org/10.1093/nsr/nwx117>
- Li, Z., Lau, W. K. M., Ramanathan, V., Wu, G., Ding, Y., Manoj, M. G., et al. (2016). Aerosol and monsoon climate interactions over Asia. *Reviews of Geophysics*, 54(4), 866–929. <https://doi.org/10.1002/2015RG000500>
- Li, Z., Li, K., Li, D., Yang, J., Xu, H., Goloub, P., & Victor, S. (2016). Simple transfer calibration method for a Cimel sun-moon photometer: Calculating lunar calibration coefficients from sun calibration coefficients from sun calibration constants. *Applied Optics*, 55(27), 7624–7630. <https://doi.org/10.1364/AO.55.007624>
- Liu, G., Li, J., Li, J., Yue, S., & Zhou, R. (2024). Estimation of nighttime aerosol optical depths using atmospheric infrared sounder longwave radiances. *Geophysical Research Letters*, 51(8), e2023GL108120. <https://doi.org/10.1029/2023GL108120>
- Lopatin, A., Dubovik, O., Fuertes, D., Stenchikov, G., Lapyonok, T., Veselovskii, I., et al. (2021). Synergy processing of diverse ground-based remote sensing and in situ data using the GRASP algorithm: Applications to radiometer, lidar and radiosonde observations. *Atmospheric Measurement Techniques*, 14(3), 2575–2614. <https://doi.org/10.5194/amt-14-2575-2021>
- Ma, J., Bi, J., Li, B., Zhu, D., Wang, X., Meng, Z., & Shi, J. (2024). Aerosol vertical structure and optical properties during two dust and haze episodes in a typical valley basin city, Lanzhou of northwest China. *Remote Sensing*, 16(5), 929. <https://doi.org/10.3390/rs16050929>
- O'Neill, N. T., Dubovik, O., & Eck, T. F. (2001). A modified Ångström coefficient for the characterization of sub-micron aerosols. *Applied Optics*, 40(15), 2368–2374. <https://doi.org/10.1364/ao.40.002368>
- O'Neill, N. T., Eck, T. F., Smirnov, A., Holben, B. N., & Thulasiraman, S. (2003). Spectral discrimination of coarse and fine mode optical depth. *Journal of Geophysical Research*, 108(D17), 4559–4573. <https://doi.org/10.1029/2002JD002975>
- Pachenko, M. V., Terpigova, S. A., Bodhaine, B. A., Isakov, A., Sviridenkov, M., Sokolik, I., et al. (1993). Optical investigations of dust storms during U.S.S.R.-U.S. experiments in Tadzhikistan, 1989. *Atmospheric Environment*, 27A(16), 2503–2508. [https://doi.org/10.1016/0960-1686\(93\)90022-q](https://doi.org/10.1016/0960-1686(93)90022-q)
- Pérez-Ramírez, D., Lyamani, H., Olmo, F. J., Whiteman, D. N., Navas-Guzmán, F., & Alados-Arboledas, L. (2012). Cloud screening and quality control algorithm for star photometer data: Assessment with lidar measurements and with all-sky images. *Atmospheric Measurement Techniques*, 5(7), 1585–1599. <https://doi.org/10.5194/amt-5-1585-2012>
- Perrone, M. R., Lorusso, A., & Romano, S. (2022). Diurnal and nocturnal aerosol properties by AERONET sun-sky-lunar photometer measurements along four years. *Atmospheric Research*, 265, 105889. <https://doi.org/10.1016/j.atmosres.2021.105889>
- Qian, Y., Yasunari, T. J., Doherty, S. J., Flanner, M. G., Lau, W. K. M., Ming, J., et al. (2014). Light-absorbing particles in snow and ice: Measurement and modeling of climatic and hydrological Impact. *Advances in Atmospheric Sciences*, 32(1), 64–91. <https://doi.org/10.1007/s00376-014-0010-0>
- Román, R., González, R., Toledano, C., Barreto, Á., Pérez-Ramírez, D., Benavent-Oltra, J. A., et al. (2020). Correction of a lunar-irradiance model for aerosol optical depth retrieval and comparison with a star photometer. *Atmospheric Measurement Techniques*, 13(11), 6293–6310. <https://doi.org/10.5194/amt-13-6293-2020>
- Rosenfeld, D., Lohmann, U., Raga, G. B., O'Dowd, C. D., Kulmala, M., Fuzzi, S., et al. (2008). Flood or drought: How do aerosols affect precipitation? *Science*, 321(5894), 1309–1313. <https://doi.org/10.1126/science.1160606>
- Rupakheti, D., Rupakheti, M., Abdullaev, S. F., Yin, X., & Kang, S. (2020). Columnar aerosol properties and radiative effects over Dushanbe, Tajikistan in Central Asia. *Environmental Pollution*, 265, 114872. <https://doi.org/10.1016/j.envpol.2020.114872>
- Schuster, G. L., Dubovik, O., & Holben, B. N. (2006). Angstrom exponent and bimodal aerosol size distributions. *Journal of Geophysical Research*, 111(D7), D07207. <https://doi.org/10.1029/2005JD006328>
- Smirnov, A., Holben, B. N., Eck, T. F., Dubovik, O., & Slutsker, I. (2000). Cloud screening and quality control algorithms for the AERONET database. *Remote Sensing of Environment*, 73(3), 337–349. [https://doi.org/10.1016/s0034-4257\(00\)00109-7](https://doi.org/10.1016/s0034-4257(00)00109-7)
- Smirnov, A., Holben, B. N., Eck, T. F., Slutsker, I., Chatenet, B., & Pinker, R. T. (2002). Diurnal variability of aerosol optical depth observed at AERONET (Aerosol Robotic Network) sites. *Geophysical Research Letters*, 29(23), 2115. <https://doi.org/10.1029/2002GL016305>
- Smirnov, V. V., Johnson, T. C., Krapivtseva, G. M., Krivchikova, T. V., & Shukurov, A. (1993). Synoptic meteorological conditions during the U. S.S.R./U.S. dust experiment in Tadzhikistan in September 1989. *Atmospheric Environment*, 27A(16), 2471–2479. [https://doi.org/10.1016/0960-1686\(93\)90018-t](https://doi.org/10.1016/0960-1686(93)90018-t)
- Sokolik, I., & Golitsyn, G. (1993). Investigation of optical and radiative properties of atmospheric dust aerosols. *Atmospheric Environment*, 27A(16), 2509–2517. [https://doi.org/10.1016/0960-1686\(93\)90023-r](https://doi.org/10.1016/0960-1686(93)90023-r)
- Song, J., Xia, X., Che, H., Wang, J., Zhang, X., & Li, X. (2018). Daytime variation of aerosol optical depth in North China and its impact on aerosol direct radiative effects. *Atmospheric Environment*, 182, 31–40. <https://doi.org/10.1016/j.atmosenv.2018.03.024>
- Sviridenkov, M. A., Gillette, D. A., Isakov, A. A., Sokolik, I., Smirnov, V., Belan, B., et al. (1993). Size distributions of dust aerosol measured during the Soviet-American experiment in Tadzhikistan, 1989. *Atmospheric Environment*, 27A(16), 2481–2486. [https://doi.org/10.1016/0960-1686\(93\)90019-u](https://doi.org/10.1016/0960-1686(93)90019-u)

- Tao, W.-K., Chen, J.-P., Li, Z., Wang, C., & Zhang, C. (2012). Impact of aerosols on convective clouds and precipitation. *Reviews of Geophysics*, 50(2), RG2001. <https://doi.org/10.1029/2011RG000369>
- Torres, B., Dubovik, O., Fuertes, D., Schuster, G., Cachorro, V. E., Lapyonok, T., et al. (2017). Advanced characterisation of aerosol size properties from measurements of spectral optical depth using the GRASP algorithm. *Atmospheric Measurement Techniques*, 10, 3743–3781. <https://doi.org/10.5194/amt-10-3743-2017>
- Uchiyama, A., Shiobara, M., Kobayashi, H., Matsunaga, T., Yamazaki, A., Inei, K., et al. (2019). Nocturnal aerosol optical depth measurements with modified sky radiometer POM-02 using the moon as a light source. *Atmospheric Measurement Techniques*, 12, 6465–6488. <https://doi.org/10.5194/amt-12-6465-2019>
- Wang, J., Xia, X., Wang, P., & Christopher, S. A. (2004). Diurnal variability of dust aerosol optical thickness and Angstrom exponent over dust source regions in China. *Geophysical Research Letters*, 31(8), L08107. <https://doi.org/10.1029/2004GL019580>
- Wang, X. (2024). The data entitled Diurnal and nocturnal dust aerosol characteristics at Ayvaj of southwest Tajikistan determined from sun-sky-lunar photometric measurements. *figshare*. [Dataset]. <https://doi.org/10.6084/m9.figshare.27889977.v1>
- Wang, Z., Liu, D., Wang, Y., Wang, Z., & Shi, G. (2015). Diurnal aerosol variations do affect daily averaged radiative forcing under heavy aerosol loading observed in Hefei, China. *Atmospheric Measurement Techniques*, 8(7), 2901–2907. <https://doi.org/10.5194/amt-8-2901-2015>
- Wehrli, C. (1985). *Extraterrestrial solar spectrum, publication no. 615*. Physikalisch-Meteorologisches Observatorium+World Radiation Center, Davos Dorf, Switzerland. Retrieved from <https://www.nrel.gov/grid/solar-resource/spectra-wehrli.html> July 1985.
- Wehrli, C. (1986). *Spectral solar irradiance data, WMO ITD 149*. WMO.
- World Health Organization. (2005). *Air quality Guidelines for particulate matter, ozone, nitrogen dioxide and sulfur dioxide. Global update, E87950*. World Health Organization Regional Office for Europe.
- Xi, X., & Sokolik, I. N. (2016). Dust interannual variability and trend in Central Asia from 2000 to 2014 and their climatic linkages. *Journal of Geophysical Research: Atmospheres*, 120(23), 12175–12197. <https://doi.org/10.1002/2015JD024092>
- Xu, H., Guo, J., Ceamanos, X., Roujean, J. L., Min, M., & Carrer, D. (2016). On the influence of the diurnal variations of aerosol content to estimate direct aerosol radiative forcing using MODIS data. *Atmospheric Environment*, 141, 186–196. <https://doi.org/10.1016/j.atmosenv.2016.06.067>
- Yu, H., Dickinson, R. E., Chin, M., Kaufman, Y., Zhou, M., Zhou, L., et al. (2004). Direct radiative effect of aerosols as determined from a combination of MODIS retrievals and GOCART simulations. *Journal of Geophysical Research*, 109(D3), D03206. <https://doi.org/10.1029/2003JD003914>
- Zhang, C., Yan, M., Du, H., Ban, J., Chen, C., Liu, Y., & Li, T. (2023). Mortality risks from a spectrum of causes associated with sand and dust storms in China. *Nature Communications*, 14(1), 6867. <https://doi.org/10.1038/s41467-023-42530-w>
- Zhang, J., Reid, J. S., Miller, S. D., & Turk, F. J. (2008). Strategy for studying nocturnal aerosol optical depth using artificial lights. *International Journal of Remote Sensing*, 29(16), 4599–4613. <https://doi.org/10.1080/01431160802020528>
- Zhang, S., Huang, Z., Li, M., Shen, X., Wang, Y., Dong, Q., et al. (2022). Vertical structure of dust aerosols observed by a ground-based Raman lidar with polarization capabilities in the center of the Taklimakan desert. *Remote Sensing*, 14(10), 2461. <https://doi.org/10.3390/rs14102461>
- Zhang, Y., Yu, H., Eck, T. F., Smirnov, A., Chin, M., Remer, L. A., et al. (2012). Aerosol daytime variations over North and South America derived from multiyear AERONET measurements. *Journal of Geophysical Research*, 117(D5), D05211. <https://doi.org/10.1029/2011JD017242>